PHYSICAL REVIEW D VOLUME 51, NUMBER 12 15 JUNE 1995

Relativistic plasmas near a Schwarzschild black hole: A solution of the two fluid ODE's in Schwarzschild coordinates

V. Buzzi and K. C. Hines
School of Physics, University of Melbourne, Parkville Victoria 3052, Australia

(Received 16 May 1994)

The 3 + 1 formalism of Thorne and Macdonald has been used to derive the linear two fluid equations describing the plasma surrounding a Schwarzschild black hole. These fluid equations lead to a set of ordinary differential equations for each of the transverse and longitudinal waves as well as for the two stream instability. The perturbations of density, velocity, and electromagnetic fields are obtained as functions of the radial coordinate r. Preliminary results are obtained for some simple cases by solving these sets of ODE's numerically as initial value problems with boundary conditions imposed at "radial infinity." The results for the electric and magnetic field perturbations are rapidly oscillating functions of the radial coordinate where the rate of oscillation largely depends on the plasma and cyclotron frequencies which are also r dependent. From the results obtained for the perturbations the average electromagnetic energy densities are computed for the Alfvén, high-frequency electromagnetic and longitudinal waves as well as the two-stream instability.

PACS number(s): 95.30.Qd, 95.30.Sf, 97.60.Lf

I. INTRODUCTION

The investigation of plasmas in the black hole environment is important because a successful study of the waves and emissions from plasma falling into a black hole will be of great value in aiding the observational identification of black hole candidates. As a result, we have begun the development of a program of black hole plasma physics with the treatment of linear waves in the two-fluid plasma [1,2] (referred to hereafter as papers I and II, where further background material may be found). The investigations contained in these two papers, for the region surrounding a Schwarzschild black hole, are limited to the "so-called" local approximation and culminate in approximate analytical expressions for the dispersion relations of plasma waves together with a numerical analysis of the modes.

The aim of the present work is to continue the investigation, above, of the behavior of plasma waves near a Schwarzschild black hole. As explained in paper I, the development of the 3 + 1 formulation of general relativity by Thorne *et al.* [3] provides a means by which the electrodynamic equations and the plasma physics look somewhat similar to the usual formulations in flat spacetime while taking accurate account of general relativistic effects such as curvature. Reference to other work in astrophysics using the 3 + 1 approach is also made in the Introduction of paper I.

Although the local approximation adopted in papers I and II makes it possible to obtain dispersion relations analytically, describing the various wave modes at a range of fixed values of the lapse function α, this does not lead to a complete description of the linear wave modes. In order to investigate such waves fully, a numerical solution of the linearized two-fluid equations is necessary, with appropriate boundary conditions at radial infinity, to obtain the velocity, density, and field perturbations as functions of the radial coordinate. One must, of course, also account for the evolution of the equilibrium plasma with respect to radial distance from the horizon. Only then is it possible to obtain a more complete and realistic idea of how such waves behave in the vicinity of a black hole and of how the horizon affects these waves. The principal objective of the work in this paper is to solve the linearized two-fluid equations for the perturbations as functions of the radial coordinate r and then to determine the average electromagnetic energy density for the Alfvén, high-frequency electromagnetic and longitudinal waves together with the two-stream instability.

Following papers I and II, a general relativistic version of the two-fluid formulation of plasma physics is considered using the $3+1$ formalism. The linearized treatment of plasma waves developed therein, in analogy with the special relativistic formulation by Sakai and Kawata [4] (SK), is used to investigate the nature of the waves close to the horizon of a Schwarzschild black hole. Such an investigation of wave propagation in a relativistic two-fluid plasma near a black hole is important for an understanding of plasma processes.

The work in papers I and II required the use of the Rindler coordinate system. In order to solve the two-fluid equations numerically for the velocity, density, and field perturbations, this is unnecessary as the equations can be solved using Schwarzschild coordinates. The two-fluid equations, when linearized, can be expressed as a set of ordinary differential equations (ODE's) in the radial coordinate r. This results in two sets of ODE's altogether, one for the Alfvén and high-frequency transverse waves and one for the longitudinal waves and the two-stream instability. Each set of linearized two-fluid ODE's can be solved as an initial value problem, requiring boundary conditions at radial infinity, $r \to \infty$. The Rindler coordinates would therefore be completely inappropriate as they are only valid in a region very close to the horizon, making it impossible to impose any meaningful boundary conditions at infinity.

The equations are treated here in essentially the same

0556-2821/95/51(12)/6692(22)/$06.00 ©1995 The American Physical Society

way as they were for the work in papers I and II as far as the physical description of the plasma is concerned. That is, attention is restricted to the radial direction, in this case the true radial direction denoted by the Schwarzschild coordinate r. As before, this restriction is valid as the fluid motion is essentially funneled into the radial direction by the strong gravitational field of the black hole. The evolution of the equilibrium velocities and fields is also dominated by r.

The work in this paper does not purport to be the final word on the numerical solution of the linear wave equations derived here; it is intended to be a preliminary study of the solutions. As will be discussed below, more rigorous numerical methods and more realistic boundary conditions would make for a more intensive and generalized investigation of the equations to follow.

In the present paper Sec II reviews the essential elements of the $3+1$ formalism and presents a summary of the fundamental nonlinear two-fluid equations expressing continuity, the conservation of energy and momentum, and Maxwell's equations. The one-dimensional two-fluid equations in Schwarzschild coordinates are derived in Sec. III following the technique outlined in paper I. The radial dependence of the equilibrium plasma parameters is discussed in Sec. IV. In Sec. V the linearized equations for the Alfvèn and high-frequency electromagnetic waves are derived and put into dimensionless form. The same is done for the longitudinal waves as well as for the two-stream instability in Sec. VI. The numerical method for analyzing these equations is discussed in Sec. VII along with the boundary conditions for the electric and magnetic field, density and velocity perturbations, and the equilibrium plasma parameters, together with a discussion of the frequency profiles. The results for the components of the electric and magnetic field perturbations are presented in Sec. VIII for the Alfvén, high-frequency electromagnetic, and longitudinal waves as well as for the two-stream instability. The resulting average electromagnetic energy densities for the various waves are presented in Sec. IX.

II. TWO-FLUID EQUATIONS IN 3 + 1 FORMALISM

The work in this paper, as in papers I and II, is based on the $3+1$ formulation of general relativity developed by Thorne, Price, and Macdonald (TPM) [3,5]. The basic concept behind the $3+1$ split of spacetime is to select a preferred set of spacelike hypersurfaces which form the level surfaces of a congruence of timelike curves. The choice of a particular set of these hypersurfaces constitutes a time slicing of spacetime. In this case the hypersurfaces are chosen to be those of constant universal time t. In TPM notation, the Schwarzschild spacetime element is given by

$$ds^2 = g_{\mu\nu}dx^\mu dx^\nu = -\left(1-\frac{2M}{r}\right)dt^2 + \frac{1}{(1-2M/r)}dr^2 + r^2\left(d\theta^2+\sin^2\theta d\phi^2\right) , \tag{1}$$

where the components x^μ denote spacetime coordinates and indices range over $0,1,2,3$. These hypersurfaces of constant universal time t define an absolute three-dimensional space described by the metric

$$ds^2 = g_{jk}dx^j dx^k = \frac{1}{(1-2M/r)}dr^2 + r^2\left(d\theta^2+\sin^2\theta d\phi^2\right) , \tag{2}$$

where the indices i,j,k refer to coordinates in absolute space and range over $1,2,3$.

Consider now a set of observers at rest with respect to this absolute space. Such observers are known as fiducial observers (FIDO's). The FIDO's measure their proper time τ using clocks that they carry with them and make local measurements of physical quantities. Hence, in what follows, all quantities such as velocities $\mathbf{v}$ and fields $\mathbf{B}$ and $\mathbf{E}$ are defined as FIDO locally measured quantities and all rates as measured by the FIDO's are measured using FIDO proper time. When making these local measurements the FIDO's use a local Cartesian coordinate system that has basis vectors of unit length tangent to the coordinate lines:

$$\mathbf{e}_{\hat r} = \left(1-\frac{2M}{r}\right)^{\frac{1}{2}}\frac{\partial}{\partial r} , \quad \mathbf{e}_{\hat\theta} = \frac{1}{r}\frac{\partial}{\partial\theta} , \quad \mathbf{e}_{\hat\phi} = \frac{1}{r\sin\theta}\frac{\partial}{\partial\phi} . \tag{3}$$

The ratio of the rate of FIDO proper time to that of universal time is defined in terms of a redshift factor known as the *lapse* function,

$$\alpha(r) \equiv \frac{d\tau}{dt} = \left(1-\frac{2M}{r}\right)^{\frac{1}{2}} , \tag{4}$$

so called because it measures the amount of FIDO proper time which has elapsed during the passage of a unit amount of universal time. It is important to note that the FIDO proper time τ functions as a local laboratory time, where the FIDO's have the role of "local laboratories." It is not a global coordinate and does not provide a slicing of spacetime. The Schwarzschild time coordinate t is the logical choice to fulfill this role and in fact slices spacetime in the way that the FIDO's would do physically. For this reason, all subsequent equations are expressed in terms of the universal time coordinate t rather than the FIDO proper time τ.

The lapse function α plays the role of a gravitational potential as well as governing the ticking rates of clocks and redshifts. From the lapse function one can compute the gravitational acceleration felt by a FIDO:

$$\mathbf{a} = -\nabla \ln\alpha = -\frac{1}{\alpha}\frac{M}{r^2}\mathbf{e}_{\hat{r}} \,. \tag{5}$$

For a derivation of the gravitational acceleration see TPM [3] or for a generalized derivation not restricted to the Schwarzschild metric see TPM [5].

For the purposes of the present work the other aspects of the membrane paradigm, as detailed in TPM [3,5], are not required. For a more detailed and general treatment of the $3+1$ split of spacetime and the concept of a set of fiducial observers (FIDO's) see Thorne *et al.* [3]. The notation adopted throughout will be that used by TPM. In general, $G = c = k_B = 1$, cgs units will be used, and all equations are valid in a FIDO rest frame (at rest with respect to the Schwarzschild coordinates).

The nonlinear two-fluid equations will not be derived here. The reader is referred to paper I [1] for a derivation of these equations from the fundamental equations expressing conservation of energy and momentum and Maxwell's equations in their $3+1$ form. In what follows, the fluid density is given by n_s, v_s is the fluid velocity, the pressure is defined by P_s, the temperature is given by T_s, charge is denoted by q_s, ε_s is the internal energy density, γ_g is the gas constant, and γ_s is the relativistic Lorentz factor. The electric and magnetic fields are denoted by $\mathbf{E}$ and $\mathbf{B}$, respectively.

In summary, recall from paper I that the continuity equation in its $3+1$ form is given by

$$\frac{\partial}{\partial t}(\gamma_s n_s) + \nabla\cdot(\alpha\gamma_s n_s \mathbf{v}_s) = 0 \,, \tag{6}$$

where s is the species index, 1 for electrons and 2 for positrons (or ions). The equations for the conservation of energy and momentum for each species s are given, respectively, by

$$\frac{1}{\alpha}\frac{\partial}{\partial t}P_s - \frac{1}{\alpha}\frac{\partial}{\partial t}\left[\gamma_s^2\left(\varepsilon_s + P_s\right)\right] - \nabla\cdot\left[\gamma_s^2\left(\varepsilon_s + P_s\right)\mathbf{v}_s\right] + \gamma_s q_s n_s \mathbf{E}\cdot\mathbf{v}_s + 2\gamma_s^2\left(\varepsilon_s + P_s\right)\mathbf{a}\cdot\mathbf{v}_s = 0 \tag{7}$$

and

$$\gamma_s^2\left(\varepsilon_s + P_s\right)\left(\frac{1}{\alpha}\frac{\partial}{\partial t} + \mathbf{v}_s\cdot\nabla\right)\mathbf{v}_s + \nabla P_s - \gamma_s q_s n_s\left(\mathbf{E} + \mathbf{v}_s\times\mathbf{B}\right)$$

$$+\mathbf{v}_s\left(\gamma_s q_s n_s \mathbf{E}\cdot\mathbf{v}_s + \frac{1}{\alpha}\frac{\partial}{\partial t}P_s\right) + \gamma_s^2\left(\varepsilon_s + P_s\right)\left(\mathbf{v}_s\left(\mathbf{v}_s\cdot\mathbf{a}\right) - \mathbf{a}\right) = 0 \,. \tag{8}$$

Maxwell's equations, coupling the two-fluid plasma to the electromagnetic fields, take the $3+1$ form

$$\nabla\cdot\mathbf{B} = 0 \,, \tag{9}$$

$$\nabla\cdot\mathbf{E} = 4\pi\sigma \,, \tag{10}$$

$$\frac{\partial\mathbf{B}}{\partial t} = -\nabla\times(\alpha\mathbf{E}) \,, \tag{11}$$

$$\frac{\partial\mathbf{E}}{\partial t} = \nabla\times(\alpha\mathbf{B}) - 4\pi\alpha\mathbf{J} \,, \tag{12}$$

where the charge and current densities are defined as

$$\sigma = \sum_s \gamma_s q_s n_s \,, \qquad \mathbf{J} = \sum_s \gamma_s q_s n_s \mathbf{v}_s \,. \tag{13}$$

In the above equations the fluid velocities and fields are all FIDO measured quantities whereas the fluid densities and pressures are measured in the rest frame of the fluid.

III. RESTRICTION TO ONE-DIMENSIONAL WAVE PROPAGATION AND LINEARIZATION

The derivation of the one-dimensional two-fluid equations in Schwarzschild coordinates follows directly from the coordinate-independent one-dimensional equations obtained in Sec. IV of paper I. To begin with, the fields, velocities, and densities are split into longitudinal and transverse components in Schwarzschild coordinates. In analogy with Eq. (26) of paper I define

$$\begin{aligned} v_{sr}(r,t) &= u_s(r,t) \,, & v_s(r,t) &= v_{s\theta}(r,t) + i v_{s\phi}(r,t) \,, \\ B(r,t) &= B_\theta(r,t) + iB_\phi(r,t) \,, & E(r,t) &= E_\theta(r,t) + iE_\phi(r,t) \,. \end{aligned} \tag{14}$$

The linearized two-fluid equations for the transverse and longitudinal waves are derived in the same way as in Sec. IV of paper I using the definitions

$$\begin{aligned} u_s(r,t) &= u_{0s}(r) + \delta u_s(r,t) \,, & v_s(r,t) &= \delta v_s(r,t) \,, \\ n_s(r,t) &= n_{0s}(r) + \delta n_s(r,t) \,, & P_s(r,t) &= P_{0s}(r) + \delta P_s(r,t) \,, \\ \rho_s(r,t) &= \rho_{0s}(r) + \delta\rho_s(r,t) \,, & \mathbf{E}_r(r,t) &= \delta\mathbf{E}_r(r,t) \,, \quad \mathbf{E}(r,t) = \delta\mathbf{E}(r,t) \,, \\ \mathbf{B}_r(r,t) &= \mathbf{B}_0(r) + \delta\mathbf{B}_r(r,t) \,, & \mathbf{B}(r,t) &= \delta\mathbf{B}(r,t) \,. \end{aligned} \tag{15}$$

IV. RADIAL DEPENDENCE OF EQUILIBRIUM PARAMETERS

The dependence of the equilibrium field and fluid parameters on the radial coordinate has already been discussed in paper I. The equilibrium parameters were expressed in terms of their limiting horizon values. In what follows, the equilibrium fields and fluid quantities are expressed in terms of their values at some large maximum value of r which corresponds numerically to an approximate radial "infinity," denoted by r_∞. This is essentially an alternative to expressing the equilibrium parameters in terms of their limiting horizon values. They are expressed here in terms of their values at radial infinity only because the boundary conditions are imposed there for the perturbations and thus it is both simpler and more consistent to describe the equilibrium field, density, and temperature profiles in terms of their values at this boundary.

Recall from paper I that the conservation of rest mass gives $r^2\alpha\gamma_{0s}n_{0s}u_{0s} = \text{const}$. It therefore follows that, in general,

$$n_{0s}(r) = n_{\infty s}\left(\frac{\alpha_\infty\gamma_{\infty s}}{\alpha\gamma_{0s}}\right)\left(\frac{u_{\infty s}}{u_{0s}}\right)\left(\frac{r_\infty}{r}\right)^2 . \tag{16}$$

For fluids in freefall so that $u_{0s} = \sqrt{r_H/r}$, this simplifies to

$$n_{0s}(r) = n_{\infty s}\left(\frac{r_\infty}{r}\right)^{\frac{3}{2}} . \tag{17}$$

From this it follows that the temperature becomes

$$T_{0s}(r) = T_{\infty s}\left(\frac{\alpha_\infty\gamma_{\infty s}}{\alpha\gamma_{0s}}\right)^{\gamma_g-1}\left(\frac{u_{\infty s}}{u_{0s}}\right)^{\gamma_g-1}\left(\frac{r_\infty}{r}\right)^{2(\gamma_g-1)} \tag{18}$$

and

$$P_{0s}(r) = P_{\infty s}\left(\frac{\alpha_\infty\gamma_{\infty s}}{\alpha\gamma_{0s}}\right)^{\gamma_g}\left(\frac{u_{\infty s}}{u_{0s}}\right)^{\gamma_g}\left(\frac{r_\infty}{r}\right)^{2\gamma_g} , \tag{19}$$

which, for fluids in freefall, simplify to

$$T_{0s}(r) = T_{\infty s}\left(\frac{r_\infty}{r}\right)^{\frac{3}{2}(\gamma_g-1)} , \quad P_{0s}(r) = P_{\infty s}\left(\frac{r_\infty}{r}\right)^{\frac{3\gamma_g}{2}} . \tag{20}$$

It can be assumed that, at radial infinity, $\alpha_\infty = \gamma_{\infty s} = 1$ because, strictly speaking, $u_{0s} = 0$ there. In fact, as will be shown below, the boundary conditions assume this to be the case. Although this is not numerically true, it is assumed to be true as a first approximation to coincide with the boundary conditions that will be used. The equilibrium magnetic field can be inferred directly from the conservation of flux, $r^2B_0(r) = \text{const}$, and is simply

$$B_0(r) = B_\infty\left(\frac{r_\infty}{r}\right)^2 . \tag{21}$$

The derivatives follow directly from the above. First, since $v_{\text{ff}}(r) = \sqrt{r_H/r}$, it follows that

$$\frac{1}{v_{\text{ff}}}\frac{dv_{\text{ff}}}{dr} = -\frac{1}{2r} . \tag{22}$$

The derivative of the number density is found to be

$$Dn_{0s} \equiv \frac{1}{n_{0s}}\frac{dn_{0s}}{dr} = -\frac{1}{2\alpha^2 r}\left(1+3\alpha^2\right) - \gamma_{0s}^2 Du_{0s} , \tag{23}$$

where Du_{0s} is the velocity derivative given by

$$Du_{0s} \equiv \frac{1}{v_{\text{ff}}}\frac{dv_{\text{ff}}}{dr} = -\frac{1}{2r} \tag{24}$$

for fluids in freefall. In the case of the two-stream instability the fluid velocities have a counterstreaming component and are given by

$$v_{0s} = \frac{(v_{\text{ff}} + \eta_s v_0)}{(1+\eta_s v_0 v_{\text{ff}})} , \eta_s = \begin{cases} -1, & s=1 \\ +1, & s=2 \end{cases}$$

From this it follows that the velocity derivative is given by

$$Dv_{0s} = \frac{1}{v_{0s}}\frac{dv_{0s}}{dr} = -\frac{1}{2r}\frac{\left(1-\eta_s\beta v_{\text{ff}}^2\right)}{\left(1+\eta_s\beta v_{\text{ff}}^2\right)} , \tag{25}$$

where it is assumed that $v_0 = \beta v_{\text{ff}}$ and β is a constant such that $\beta \leq 1$. Finally, the derivative of the equilibrium magnetic field is simply

$$DB_0 = \frac{1}{B_0}\frac{dB_0}{dr} = -\frac{2}{r} . \tag{26}$$

V. LINEARIZED EQUATIONS FOR THE TRANSVERSE WAVES IN SCHWARZSCHILD COORDINATES

For any vector $\mathbf{A}(r)$ and scalar $\Psi(r)$, independent of the spatial coordinates θ and ϕ, it is true that

$$\nabla\Psi = \alpha\frac{\partial\Psi}{\partial r} , \qquad \nabla\cdot\mathbf{A} = \frac{\alpha}{r^2}\frac{\partial}{\partial r}\left(r^2 A_r\right) ,$$
$$\nabla\times\mathbf{A} = -\frac{\alpha}{r}\frac{\partial}{\partial r}\left(rA_\phi\right)\mathbf{e}_{\hat\theta} + \frac{\alpha}{r}\frac{\partial}{\partial r}\left(rA_\theta\right)\mathbf{e}_{\hat\phi} . \tag{27}$$

Hence, the gravitational acceleration in Schwarzschild coordinates is given by

$$a = -\frac{1}{\alpha}|\nabla\alpha| = -\frac{d\alpha}{dr} = -\frac{r_H}{2\alpha r^2} . \tag{28}$$

The fluid equations and Maxwell's equations in Schwarzschild coordinates are derived in the same way as those in terms of Rindler coordinates in Sec. IV of paper I. The nonlinear equations in Schwarzschild coordinates are therefore given by

$$\frac{1}{\alpha}\frac{\partial B}{\partial t} = -\frac{i}{r}\frac{\partial}{\partial r}\left(r\alpha E\right) , \tag{29}$$

$$\frac{\alpha}{r}\frac{\partial}{\partial r}\left(r\alpha B\right) = -i\frac{\partial E}{\partial t} - i4\pi e\alpha\left(\gamma_2 n_2 v_2 - \gamma_1 n_1 v_1\right) , \tag{30}$$

and

$$\rho_s\left(\frac{1}{\alpha}\frac{\partial}{\partial t}+\alpha u_s\frac{\partial}{\partial r}\right)v_s=q_s n_s\gamma_s\left(E-iv_sB_r+iu_sB\right)-\rho_s u_s v_s a-\ v_s\left(q_s n_s\gamma_s\mathbf{E}\cdot\mathbf{v}_s+\frac{1}{\alpha}\frac{\partial P_s}{\partial t}\right)\,. \tag{31}$$

These three equations are the Schwarzschild coordinate equivalents of Eqs. (32), (33), and (35) of paper I. When linearized and Fourier transformed with respect to universal time t, they take the form

$$\frac{d}{dr}\left(\alpha\delta E\right)=\frac{\alpha}{r}\delta E+\frac{\omega}{\alpha}\delta B\,, \tag{32}$$

$$\frac{d}{dr}\left(\alpha\delta B\right)=-\frac{\alpha}{r}\delta B-\frac{\omega}{\alpha}\delta E-i4\pi e\left(\gamma_{02}n_{02}\delta v_2-\gamma_{01}n_{01}\delta v_1\right)\ , \tag{33}$$

and

$$\alpha\frac{d\delta v_s}{dr}=\frac{1}{u_{0s}}\left(\frac{u_{0s}r_H}{2\alpha r^2}+\frac{i\omega}{\alpha}-\frac{iq_s\gamma_{0s}n_{0s}B_0}{\rho_s}\right)\delta v_s+\frac{q_s\gamma_{0s}n_{0s}}{\rho_s u_{0s}}\left(\delta E-iu_{0s}\delta B\right)\,. \tag{34}$$

The perturbations are now scaled by α and their equilibrium values so that it is possible to define dimensionless perturbations as

$$\delta\widetilde{B}\equiv\frac{\alpha\delta B}{B_0},\quad \delta\widetilde{E}\equiv\frac{\alpha\delta E}{B_0},\quad\text{and}\quad \delta\tilde{v}_s\equiv\frac{\alpha\delta v_s}{u_{0s}}. \tag{35}$$

It follows therefore that, for any perturbation $\delta\Psi$,

$$\alpha\frac{d\delta\Psi}{dr}=\Psi_{0s}\frac{d\delta\widetilde{\Psi}}{dr}-\Psi_{0s}\left(\frac{r_H}{2\alpha^2r^2}-D\Psi_{0s}\right)\delta\widetilde{\Psi}\,, \tag{36}$$

where

$$D\Psi_{0s}\equiv\frac{1}{\Psi_{0s}}\frac{d\Psi_{0s}}{dr}$$

as usual.

The reason for scaling the transverse fields and velocities by α is that these transverse fields tend to $1/\alpha$ as $\alpha\to 0$ and so diverge at the horizon [3]. Scaling them by α ensures that they will be finite as they approach the horizon. Define also

$$\tilde{r}\equiv\frac{r}{r_H},\quad \tilde{\omega}\equiv\frac{\omega}{\alpha\omega_*}\ ,\quad\text{and}\quad k_H=\frac{1}{r_H\omega_*}\ , \tag{37}$$

so that, for any equilibrium quantity Ψ_{0s},

$$D\widetilde{\Psi}_{0s}\equiv\frac{1}{\Psi_{0s}}\frac{d\Psi_{0s}}{d\tilde{r}}=r_HD\Psi_{0s}\,.$$

The set of four complex equations is given by

$$\frac{d\delta\tilde{v}_s}{d\tilde{r}}=\left[\frac{1}{\alpha^2\tilde{r}^2}-D\tilde{u}_{0s}+\frac{i}{\alpha k_Hu_{0s}}\left(\tilde{\omega}-\frac{q_s}{e}\frac{\omega_{cs}}{\omega_*}\right)\right]\delta\tilde{v}_s+\left(\frac{q_s}{e}\right)\frac{1}{\alpha k_Hu_{0s}^2}\frac{\omega_{cs}}{\omega_*}\left(\delta\widetilde{E}-iu_{0s}\delta\widetilde{B}\right) \tag{38}$$

for each species $s=1,2,$

$$\frac{d\delta\widetilde{B}}{d\tilde{r}}=-\left(\frac{1}{\tilde{r}}+D\widetilde{B}_0\right)\delta\widetilde{B}-\frac{\tilde{\omega}}{\alpha k_H}\delta\widetilde{E}+\frac{i}{\alpha k_H\omega_*}\left(u_{01}\frac{\omega_{p1}^2}{\omega_{c1}}\delta\tilde{v}_1-u_{02}\frac{\omega_{p2}^2}{\omega_{c2}}\delta\tilde{v}_2\right) \tag{39}$$

and

$$\frac{d\delta\widetilde{E}}{d\tilde{r}}=-\left(\frac{1}{\tilde{r}}+D\widetilde{B}_0\right)\delta\widetilde{E}+\frac{\tilde{\omega}}{\alpha k_H}\delta\widetilde{B}\,, \tag{40}$$

where

$$D\tilde{u}_{0s}=-\frac{1}{2\tilde{r}}\quad\text{and}\quad D\widetilde{B}_0=-\frac{2}{\tilde{r}}\,.$$

Defining the perturbations in terms of their real (R) and imaginary (I) components,

$$\delta\tilde{v}_s=\delta\tilde{v}_{sR}+i\delta\tilde{v}_{sI}\,,\quad \delta\widetilde{B}=\delta\widetilde{B}_R+i\delta\widetilde{B}_I,$$

$$\delta\widetilde{E}=\delta\widetilde{E}_R+i\delta\widetilde{E}_I\ , \tag{41}$$

Eqs. (38)–(40) can be written as a set of eight purely real equations as follows:

$$\frac{d\delta\tilde{v}_{sR}}{d\tilde{r}}=\left(\frac{1}{\alpha^2\tilde{r}^2}+\frac{1}{2\tilde{r}}\right)\delta\tilde{v}_{sR}-\frac{1}{\alpha k_Hu_{0s}}\left(\tilde{\omega}-\frac{q_s}{e}\frac{\omega_{cs}}{\omega_*}\right)\delta\tilde{v}_{sI}+\left(\frac{q_s}{e}\right)\frac{1}{\alpha k_Hu_{0s}^2}\frac{\omega_{cs}}{\omega_*}\left(\delta\widetilde{E}_R+u_{0s}\delta\widetilde{B}_I\right)\ , \tag{42}$$

$$\frac{d\delta\tilde{v}_{sI}}{d\tilde{r}}=\frac{1}{\alpha k_Hu_{0s}}\left(\tilde{\omega}-\frac{q_s}{e}\frac{\omega_{cs}}{\omega_*}\right)\delta\tilde{v}_{sR}+\left(\frac{1}{\alpha^2\tilde{r}^2}+\frac{1}{2\tilde{r}}\right)\delta\tilde{v}_{sI}+\left(\frac{q_s}{e}\right)\frac{1}{\alpha k_Hu_{0s}^2}\frac{\omega_{cs}}{\omega_*}\left(\delta\widetilde{E}_I-u_{0s}\delta\widetilde{B}_R\right)\ , \tag{43}$$

$$\frac{d\delta\widetilde{B}_R}{d\tilde{r}}=\frac{1}{\alpha k_H\omega_*}\left(u_{02}\frac{\omega_{p2}^2}{\omega_{c2}}\delta\tilde{v}_{2I}-u_{01}\frac{\omega_{p1}^2}{\omega_{c1}}\delta\tilde{v}_{1I}\right)+\frac{1}{\tilde{r}}\delta\widetilde{B}_R-\frac{\tilde{\omega}}{\alpha k_H}\delta\widetilde{E}_R\,, \tag{44}$$

$$\frac{d\delta\widetilde{B}_I}{d\tilde{r}} = \frac{1}{\alpha k_H \omega_*}\left(u_{01}\frac{\omega_{p1}^2}{\omega_{c1}}\delta\tilde{v}_{1R} - u_{02}\frac{\omega_{p2}^2}{\omega_{c2}}\delta\tilde{v}_{2R}\right) + \frac{1}{\tilde{r}}\delta\widetilde{B}_I - \frac{\tilde{\omega}}{\alpha k_I}\delta\widetilde{E}_I \,, \tag{45}$$

$$\frac{d\delta\widetilde{E}_R}{d\tilde{r}} = \frac{\tilde{\omega}}{\alpha k_H}\delta\widetilde{B}_R - \frac{1}{\tilde{r}}\delta\widetilde{E}_R \,, \tag{46}$$

and

$$\frac{d\delta\widetilde{E}_I}{d\tilde{r}} = \frac{\tilde{\omega}}{\alpha k_H}\delta\widetilde{B}_I - \frac{1}{\tilde{r}}\delta\widetilde{E}_I \,. \tag{47}$$

In the above equations, ω_* is given by

$$\omega_* = \begin{cases} \frac{1}{\sqrt{2}}\left(\omega_{c1}^2 + \omega_{c2}^2\right)^{\frac{1}{2}}, & \text{Alfvén modes,} \\ \frac{1}{\sqrt{2}}\left(\omega_{*1}^2 + \omega_{*2}^2\right)^{\frac{1}{2}}, & \text{high-frequency modes,} \end{cases} \tag{48}$$

where $\omega_{*s} = \left(2\omega_{ps}^2 + \omega_{cs}^2\right)^{\frac{1}{2}}$.

The following definitions may also be useful:

$$\alpha = \left(1 - \frac{1}{\tilde{r}}\right)^{\frac{1}{2}}, \quad u_{0s} = \frac{1}{\sqrt{\tilde{r}}}, \quad k_H \equiv \frac{1}{r_H \omega_*}.$$

Finally, $\omega_{ps}^2(r) = 4\pi e^2\gamma_{0s}^2 n_{0s}^2/\rho_{0s}$ and $\omega_{cs}(r) = e\gamma_{0s}n_{0s}B_0/\rho_{0s}$ as before. Solving the above equations to find the perturbations as functions of the radial coordinate r, one can calculate the average electromagnetic energy density.

VI. LINEARIZED EQUATIONS FOR THE LONGITUDINAL WAVES IN SCHWARZSCHILD COORDINATES

The same is done for the longitudinal waves so that the nonlinear equations are given by

$$\frac{\partial}{\partial t}(\gamma_s n_s) + \frac{\alpha}{r^2}\frac{\partial}{\partial r}\left(r^2\alpha\gamma_s n_s u_s\right) = 0 \,, \tag{49}$$

$$\frac{\alpha}{r^2}\frac{\partial}{\partial r}\left(r^2 E_r\right) = 4\pi e\left(\gamma_2 n_2 - \gamma_1 n_1\right) \,, \tag{50}$$

and

$$\rho_s\left(\frac{1}{\alpha}\frac{\partial}{\partial t} + \alpha u_s\frac{\partial}{\partial r}\right)u_s = q_s\gamma_s n_s\left(E_r + \frac{i}{2}\left(v_s B^* - v_s^* B\right)\right) + \rho_s\left(1 - u_s^2\right)a - \alpha\frac{\partial}{\partial r}P_s - u_s\left(q_s\gamma_s n_s \mathbf{E}\cdot\mathbf{v}_s + \frac{1}{\alpha}\frac{\partial P_s}{\partial t}\right) . \tag{51}$$

These are the Schwarzschild equivalents to Eqs. (30), (31), and (34) of paper I. When linearized and Fourier transformed they become

$$\begin{aligned}\left(u_{0s}^2 - \frac{v_{Ts}^2}{2}\right)\frac{\alpha}{u_{0s}}\frac{d\delta u_s}{dr} = &\left\{\frac{v_{Ts}^2}{2}\frac{\left(1+3\alpha^2\right)}{2\alpha r} + \frac{i\omega u_{0s}}{\alpha}\left(1 - \frac{v_{Ts}^2}{2}\right)\right. \\ &\left. + \alpha\frac{v_{Ts}^2}{2}Dn_{0s} - \alpha u_{0s}^2\gamma_{0s}^2\left(1 + u_{0s}^2 - 3\frac{v_{Ts}^2}{2}\right)Du_{0s}\right\}\frac{\delta u_s}{u_{0s}} \\ &- \frac{1}{\gamma_{0s}^2}\left\{\frac{1}{2\alpha r}\left(1 - \alpha^2 - 2\alpha^2 v_{Ts}^2\right) + \alpha\left(\gamma_g - 1\right)\frac{v_{Ts}^2}{2}Dn_{0s}\right. \\ &\left. + \alpha\left(u_{0s}^2\gamma_{0s}^2 - \frac{v_{Ts}^2}{2}\right)Du_{0s} + \frac{i\omega}{\alpha u_{0s}\gamma_{0s}^2}\frac{v_{Ts}^2}{2}\right\}\frac{\delta n_s}{n_{0s}} + \frac{q_s n_{0s}}{\gamma_{0s}\rho_{0s}}\delta E_r \,,\end{aligned} \tag{52}$$

$$\begin{aligned}\left(u_{0s}^2 - \frac{v_{Ts}^2}{2}\right)\frac{\alpha}{n_{0s}}\frac{d\delta n_s}{dr} = &\left\{\frac{1}{2\alpha r}\left[\left(1-\alpha^2\right)\left(1 + \frac{v_{Ts}^2}{2}\right) - u_{0s}^2\left(1+3\alpha^2\right)\right]\right. \\ &\left. + \alpha u_{0s}^2\gamma_{0s}^2\frac{v_{Ts}^2}{2}Du_{0s} + \alpha\left(\gamma_g - 1\right)\frac{v_{Ts}^2}{2}Dn_{0s} + \frac{i\omega u_{0s}}{\alpha}\left(1 - \frac{v_{Ts}^2}{2}\right)\right\}\frac{\delta n_s}{n_{0s}} \\ &- u_{0s}\gamma_{0s}^2\left\{\frac{\left(1+3\alpha^2\right)}{2\alpha r} - \alpha\gamma_{0s}^2\left(1 - 2u_{0s}^2\right)Du_{0s} + \alpha Dn_{0s} + \frac{i\omega}{\alpha u_{0s}\gamma_{0s}^2}\right\}\delta u_s \\ &- \frac{q_s\gamma_{0s}n_{0s}}{\rho_{0s}}\delta E_r \,,\end{aligned} \tag{53}$$

and

$$\alpha\frac{d\delta E_r}{dr} = -\frac{2\alpha}{r}\delta E_r + 4\pi e\left(\gamma_{02}\delta n_2 - \gamma_{01}\delta n_1\right) + 4\pi e\left(n_{02}u_{02}\gamma_{02}^3\delta u_2 - n_{01}u_{01}\gamma_{01}^3\delta u_1\right) . \tag{54}$$

These equations are then made dimensionless by defining

$$\delta\tilde{n}_s \equiv \frac{\alpha\delta n_s}{n_{0s}}, \quad \delta\tilde{u}_s \equiv \frac{\alpha\delta u_s}{u_{0s}}, \quad \text{and} \quad \delta\widetilde{E}_r \equiv \frac{\alpha\delta E_r}{B_0} . \tag{55}$$

It should not be necessary to scale the longitudinal perturbations by α since the longitudinal fields should not diverge at the horizon, as $\alpha \to 0$. However, to be consistent with the notation adopted for the transverse waves and also to ensure that the fields are indeed finite at the horizon, they will also be scaled by α. Define

$$\omega_* = \left(\omega_{p1}^2 + \omega_{p2}^2\right)^{\frac{1}{2}} ,$$

which, for $\omega_p \equiv \omega_{p1} = \omega_{p2}$, reduces to $\omega_* = \sqrt{2}\omega_p$. Then, with Eq. (37), the dimensionless linear equations become

$$\begin{aligned}\frac{d\delta\tilde{u}_s}{d\tilde{r}} = {} & \frac{1}{\left(u_{0s}^2 - v_{Ts}^2/2\right)}\left\{\frac{\left(u_{0s}^2 - v_{Ts}^2/2\right)}{2\alpha^2\tilde{r}^2} + \frac{\left(1+3\alpha^2\right)}{2\alpha^2\tilde{r}}\frac{v_{Ts}^2}{2} + \frac{v_{Ts}^2}{2}D\tilde{n}_{0s}\right. \\ & \left. -\gamma_{0s}^2\left[2u_{0s}^2\left(1-\frac{v_{Ts}^2}{2}\right) - \frac{v_{Ts}^2}{2}\right]D\tilde{u}_{0s} + \frac{i\tilde{\omega}u_{0s}}{\alpha k_H}\left(1-\frac{v_{Ts}^2}{2}\right)\right\}\delta\tilde{u}_s \\ & +\frac{1}{\gamma_{0s}^2}\frac{1}{\left(u_{0s}^2 - v_{Ts}^2/2\right)}\left\{\frac{1}{2\alpha^2\tilde{r}}\left(\alpha^2 + 4\alpha^2\frac{v_{Ts}^2}{2} - 1\right) - \left(\gamma_g - 1\right)\frac{v_{Ts}^2}{2}D\tilde{n}_{0s}\right. \\ & \left. -\left(u_{0s}^2\gamma_{0s}^2 - \frac{v_{Ts}^2}{2}\right)D\tilde{u}_{0s} - \frac{i\tilde{\omega}}{\alpha u_{0s}k_H\gamma_{0s}^2}\frac{v_{Ts}^2}{2}\right\}\delta\tilde{n}_s + \left(\frac{q_s}{e}\right)\left(\frac{\omega_{cs}}{\omega_*}\right)\frac{1}{\alpha k_H\gamma_{0s}^2}\frac{1}{\left(u_{0s}^2 - v_{Ts}^2/2\right)}\delta\widetilde{E}_r ,\end{aligned} \tag{56}$$

$$\begin{aligned}\frac{d\delta\tilde{n}_s}{d\tilde{r}} = {} & \frac{1}{\left(u_{0s}^2 - v_{Ts}^2/2\right)}\left\{\frac{1}{2\alpha\tilde{r}}\left[\left(1-\alpha^2\right)\left(1+\frac{v_{Ts}^2}{2}\right) - u_{0s}^2\left(1+3\alpha^2\right)\right]\right. \\ & \left. +\frac{\left(u_{0s}^2 - v_{Ts}^2/2\right)}{2\alpha^2\tilde{r}^2} - \left(u_{0s}^2 - \gamma_g\frac{v_{Ts}^2}{2}\right)D\tilde{n}_{0s} + u_{0s}^2\gamma_{0s}^2\frac{v_{Ts}^2}{2}D\tilde{u}_{0s} + \frac{i\tilde{\omega}u_{0s}}{\alpha k_H}\left(1-\frac{v_{Ts}^2}{2}\right)\right\}\delta\tilde{n}_s \\ & -\frac{u_{0s}^2\gamma_{0s}^2}{\left(u_{0s}^2 - v_{Ts}^2/2\right)}\left\{\frac{\left(1+3\alpha^2\right)}{2\alpha^2\tilde{r}} - \gamma_{0s}^2\left(1-2u_{0s}^2\right)D\tilde{u}_{0s} + D\tilde{n}_{0s} + \frac{i\tilde{\omega}}{\alpha k_H u_{0s}\gamma_{0s}^2}\right\}\delta\tilde{u}_s \\ & -\left(\frac{q_s}{e}\right)\left(\frac{\omega_{cs}}{\omega_*}\right)\frac{1}{\alpha k_H}\frac{1}{\left(u_{0s}^2 - v_{Ts}^2/2\right)}\delta\widetilde{E}_r ,\end{aligned} \tag{57}$$

and, for the radial component of the electric field perturbation,

$$\begin{aligned}\frac{d\delta\widetilde{E}_r}{d\tilde{r}} = {} & \left(\frac{1}{2\alpha^2\tilde{r}^2} - \frac{2}{\tilde{r}} - D\widetilde{B}_0\right)\delta\widetilde{E}_r + \frac{1}{\alpha k_H\omega_*}\left(\frac{\omega_{p2}^2}{\omega_{c2}}\delta\tilde{n}_2 - \frac{\omega_{p1}^2}{\omega_{c1}}\delta\tilde{n}_1\right) \\ & +\frac{1}{\alpha k_H\omega_*}\left(\frac{\omega_{p2}^2}{\omega_{c2}}u_{02}^2\gamma_{02}^2\delta\tilde{u}_2 - \frac{\omega_{p1}^2}{\omega_{c1}}u_{01}^2\gamma_{01}^2\delta\tilde{u}_1\right) .\end{aligned} \tag{58}$$

As for the transverse waves, define

$$\delta\tilde{u}_s = \delta\tilde{u}_{sR} + i\delta\tilde{u}_{sI} , \quad \delta\tilde{n}_s = \delta\tilde{n}_{sR} + i\delta\tilde{n}_{sI}, \quad \text{and} \quad \delta\widetilde{E}_r = \delta\widetilde{E}_{rR} + i\delta\widetilde{E}_{rI} . \tag{59}$$

Thus, the resulting set of ten linear wave equations is given by

$$\begin{aligned}\frac{d\delta\tilde{u}_{sR}}{d\tilde{r}} = {} & \frac{1}{\left(u_{0s}^2 - v_{Ts}^2/2\right)}\left\{\frac{1}{2\alpha^2\tilde{r}^2}\left(u_{0s}^2 - \frac{v_{Ts}^2}{2}\right) + \frac{\left(1+3\alpha^2\right)}{2\alpha^2\tilde{r}}\frac{v_{Ts}^2}{2} + \frac{v_{Ts}^2}{2}D\tilde{n}_{0s}\right. \\ & \left. -\gamma_{0s}^2\left[2u_{0s}^2\left(1-\frac{v_{Ts}^2}{2}\right) - \frac{v_{Ts}^2}{2}\right]D\tilde{u}_{0s}\right\}\delta\tilde{u}_{sR} \\ & -\frac{\tilde{\omega}u_{0s}}{\alpha k_H}\frac{\left(1-v_{Ts}^2/2\right)}{\left(u_{0s}^2 - v_{Ts}^2/2\right)}\delta\tilde{u}_{sI} + \frac{\tilde{\omega}}{\alpha k_H u_{0s}\gamma_{0s}^4}\frac{v_{Ts}^2}{2}\frac{1}{\left(u_{0s}^2 - v_{Ts}^2/2\right)}\delta\tilde{n}_{sI} \\ & +\frac{1}{\gamma_{0s}^2}\frac{1}{\left(u_{0s}^2 - v_{Ts}^2/2\right)}\left\{\frac{1}{2\alpha^2\tilde{r}}\left(\alpha^2 + 4\alpha^2\frac{v_{Ts}^2}{2} - 1\right) - \left(\gamma_g - 1\right)\frac{v_{Ts}^2}{2}D\tilde{n}_{0s} - \left(u_{0s}^2\gamma_{0s}^2 - \frac{v_{Ts}^2}{2}\right)D\tilde{u}_{0s}\right\}\delta\tilde{n}_{sR} \\ & +\left(\frac{q_s}{e}\right)\left(\frac{\omega_{cs}}{\omega_*}\right)\frac{1}{\alpha k_H\gamma_{0s}^2}\frac{1}{\left(u_{0s}^2 - v_{Ts}^2/2\right)}\delta\widetilde{E}_{rR} ,\end{aligned} \tag{60}$$

$$\begin{aligned}\frac{d\delta\tilde{u}_{sI}}{d\tilde{r}} = {} & \frac{1}{(u_{0s}^2 - v_{Ts}^2/2)}\left\{\frac{1}{2\alpha^2\tilde{r}^2}\left(u_{0s}^2 - \frac{v_{Ts}^2}{2}\right) + \frac{\left(1+3\alpha^2\right)}{2\alpha^2\tilde{r}}\frac{v_{Ts}^2}{2} + \frac{v_{Ts}^2}{2}D\tilde{n}_{0s}\right. \\ & \left. -\gamma_{0s}^2\left[2u_{0s}^2\left(1 - \frac{v_{Ts}^2}{2}\right) - \frac{v_{Ts}^2}{2}\right]D\tilde{u}_{0s}\right\}\delta\tilde{u}_{sI} \\ & +\frac{\tilde{\omega}u_{0s}}{\alpha k_H}\frac{\left(1 - v_{Ts}^2/2\right)}{(u_{0s}^2 - v_{Ts}^2/2)}\delta\tilde{u}_{sR} - \frac{\tilde{\omega}}{\alpha k_H u_{0s}\gamma_{0s}^4}\frac{v_{Ts}^2}{2}\frac{1}{(u_{0s}^2 - v_{Ts}^2/2)}\delta\tilde{n}_{sR} \\ & +\frac{1}{\gamma_{0s}^2}\frac{1}{(u_{0s}^2 - v_{Ts}^2/2)}\left\{\frac{1}{2\alpha^2\tilde{r}}\left(\alpha^2 + 4\alpha^2\frac{v_{Ts}^2}{2} - 1\right) - (\gamma_g - 1)\frac{v_{Ts}^2}{2}D\tilde{n}_{0s} - \left(u_{0s}^2\gamma_{0s}^2 - \frac{v_{Ts}^2}{2}\right)D\tilde{u}_{0s}\right\}\delta\tilde{n}_{sI} \\ & +\left(\frac{q_s}{e}\right)\left(\frac{\omega_{cs}}{\omega_*}\right)\frac{1}{\alpha k_H\gamma_{0s}^2}\frac{1}{(u_{0s}^2 - v_{Ts}^2/2)}\delta\widetilde{E}_{rI}\,, \end{aligned} \tag{61}$$

$$\begin{aligned}\frac{d\delta\tilde{n}_{sR}}{d\tilde{r}} = {} & \frac{1}{(u_{0s}^2 - v_{Ts}^2/2)}\left\{\frac{1}{2\alpha\tilde{r}}\left[\left(1-\alpha^2\right)\left(1 + \frac{v_{Ts}^2}{2}\right) - u_{0s}^2\left(1+3\alpha^2\right)\right]\right. \\ & \left. +\frac{1}{2\alpha^2\tilde{r}^2}\left(u_{0s}^2 - \frac{v_{Ts}^2}{2}\right) + u_{0s}^2\gamma_{0s}^2\frac{v_{Ts}^2}{2}D\tilde{u}_{0s} - \left(u_{0s}^2 - \gamma_g\frac{v_{Ts}^2}{2}\right)D\tilde{n}_{0s}\right\}\delta\tilde{n}_{sR} \\ & -\frac{\tilde{\omega}u_{0s}}{\alpha k_H}\frac{\left(1 - v_{Ts}^2/2\right)}{(u_{0s}^2 - v_{Ts}^2/2)}\delta\tilde{n}_{sI} + \frac{\tilde{\omega}u_{0s}}{\alpha k_H}\frac{1}{(u_{0s}^2 - v_{Ts}^2/2)}\delta\tilde{u}_{sI} \\ & -\frac{u_{0s}^2\gamma_{0s}^2}{(u_{0s}^2 - v_{Ts}^2/2)}\left\{\frac{\left(1+3\alpha^2\right)}{2\alpha^2\tilde{r}} + D\tilde{n}_{0s} - \gamma_{0s}^2\left(1 - 2u_{0s}^2\right)D\tilde{u}_{0s}\right\}\delta\tilde{u}_{sR} \\ & -\left(\frac{q_s}{e}\right)\left(\frac{\omega_{cs}}{\omega_*}\right)\frac{1}{\alpha k_H}\frac{1}{(u_{0s}^2 - v_{Ts}^2/2)}\delta\widetilde{E}_{rR}\,, \end{aligned} \tag{62}$$

$$\begin{aligned}\frac{d\delta\tilde{n}_{sI}}{d\tilde{r}} = {} & \frac{1}{(u_{0s}^2 - v_{Ts}^2/2)}\left\{\frac{1}{2\alpha\tilde{r}}\left[\left(1-\alpha^2\right)\left(1 + \frac{v_{Ts}^2}{2}\right) - u_{0s}^2\left(1+3\alpha^2\right)\right]\right. \\ & \left. +\frac{1}{2\alpha^2\tilde{r}^2}\left(u_{0s}^2 - \frac{v_{Ts}^2}{2}\right) + u_{0s}^2\gamma_{0s}^2\frac{v_{Ts}^2}{2}D\tilde{u}_{0s} - \left(u_{0s}^2 - \gamma_g\frac{v_{Ts}^2}{2}\right)D\tilde{n}_{0s}\right\}\delta\tilde{n}_{sI} \\ & +\frac{\tilde{\omega}u_{0s}}{\alpha k_H}\frac{\left(1 - v_{Ts}^2/2\right)}{(u_{0s}^2 - v_{Ts}^2/2)}\delta\tilde{n}_{sR} - \frac{\tilde{\omega}u_{0s}}{\alpha k_H}\frac{1}{(u_{0s}^2 - v_{Ts}^2/2)}\delta\tilde{u}_{sR} \\ & -\frac{u_{0s}^2\gamma_{0s}^2}{(u_{0s}^2 - v_{Ts}^2/2)}\left\{\frac{\left(1+3\alpha^2\right)}{2\alpha^2\tilde{r}} + D\tilde{n}_{0s} - \gamma_{0s}^2\left(1 - 2u_{0s}^2\right)D\tilde{u}_{0s}\right\}\delta\tilde{u}_{sI} \\ & -\left(\frac{q_s}{e}\right)\left(\frac{\omega_{cs}}{\omega_*}\right)\frac{1}{\alpha k_H}\frac{1}{(u_{0s}^2 - v_{Ts}^2/2)}\delta\widetilde{E}_{rI}\,, \end{aligned} \tag{63}$$

$$\begin{aligned}\frac{d\delta\widetilde{E}_{rR}}{dr} = {} & \left(\frac{1}{2\alpha^2\tilde{r}^2} - \frac{2}{\tilde{r}} - D\widetilde{B}_0\right)\delta\widetilde{E}_{rR} + \frac{1}{\alpha k_H\omega_*}\left(\frac{\omega_{p2}^2}{\omega_{c2}}\delta\tilde{n}_{2R} - \frac{\omega_{p1}^2}{\omega_{c1}}\delta\tilde{n}_{1R}\right) \\ & +\frac{1}{\alpha k_H\omega_*}\left(\frac{\omega_{p2}^2}{\omega_{c2}}u_{02}^2\gamma_{02}^2\delta\tilde{u}_{2R} - \frac{\omega_{p1}^2}{\omega_{c1}}u_{01}^2\gamma_{01}^2\delta\tilde{u}_{1R}\right)\,, \end{aligned} \tag{64}$$

and

$$\begin{aligned}\frac{d\delta\widetilde{E}_{rI}}{dr} = {} & \left(\frac{1}{2\alpha^2\tilde{r}^2} - \frac{2}{\tilde{r}} - D\widetilde{B}_0\right)\delta\widetilde{E}_{rI} + \frac{1}{\alpha k_H\omega_*}\left(\frac{\omega_{p2}^2}{\omega_{c2}}\delta\tilde{n}_{2I} - \frac{\omega_{p1}^2}{\omega_{c1}}\delta\tilde{n}_{1I}\right) \\ & +\frac{1}{\alpha k_H\omega_*}\left(\frac{\omega_{p2}^2}{\omega_{c2}}u_{02}^2\gamma_{02}^2\delta\tilde{u}_{2I} - \frac{\omega_{p1}^2}{\omega_{c1}}u_{01}^2\gamma_{01}^2\delta\tilde{u}_{1I}\right)\,. \end{aligned} \tag{65}$$

The equations for the two-stream instability are exactly those for the longitudinal waves but now the velocities, densities, and their derivatives are replaced by the corresponding values for the two-stream instability. Hence, Eq. (24) is replaced by Eq. (25) and Eq. (23) is modified accordingly.

The ordinary differential equations derived here for the transverse and longitudinal waves, respectively, are now in the required form to be solved numerically in order to determine the field, velocity, and density perturbations as functions of the radial coordinate r.

VII. NUMERICAL METHOD

The sets of ordinary differential equations, described by Eqs. (42)–(47) for the transverse waves and Eqs. (60)–(65) for the longitudinal waves and the two-stream instability, are solved using the well known LSODA package [6]. LSODA solves initial value problems for stiff or nonstiff systems of first-order ODE's. It has the advantage of automatically selecting between stiff and nonstiff methods. It uses Adams methods (predictor-corrector) in the nonstiff regions and backward differentiation formula (BDF) methods when the equations become stiff. It uses the nonstiff method initially and dynamically monitors data in order to decide which method to use. If and when LSODA regards the problem as stiff and switches method accordingly, it makes use of the $N \times N$ Jacobian matrix $j = df/dy$, where N is the number of ODE's, 8 for the transverse waves and 10 for the longitudinal waves and the two-stream instability. The user has the option of simply allowing LSODA to approximate the Jacobian internally by difference quotients or of supplying the Jacobian matrix in closed form. The latter greatly reduces the number of function calls required by LSODA and so, in this case where the sets of ODE's are stiff in general, the Jacobian has been supplied in closed form.

One important point is that the LSODA package does not allow for integrating smoothly through critical points within the integration range. Although there are no critical points within the integration range for the Alfvén and high-frequency transverse waves, critical points do exist for the longitudinal waves (and, therefore, also for the two-stream instability). These critical points correspond to the transonic radius, that is, the radius at which $u_{0s}^2 = v_T^2 s/2$ for each fluid species. The cases considered in the present paper for the longitudinal waves and the two-stream instability are limited to those for which the critical points lie outside the integration range. This is closely linked with the choice of limiting values for the temperature of each fluid species, as will be shown below. Because of the preliminary nature of the present work a more general investigation of the longitudinal waves and the two-stream instability, including all possible cases, has not been included but is left to future work.

To investigate the longitudinal waves and two-stream instability more thoroughly it is necessary to make use of a numerical method which allows for critical points inside the integration range, such as the HEMODES package developed by Nobili and Turolla [7]. HEMODES is based on a generalization of the Henyey method and is specifically designed to treat systems of ordinary differential equations with one or more critical points and is particularly suited to astrophysical applications. The HEMODES package or a numerical approach very much like it is needed if a complete investigation of the longitudinal and two-stream ODE's is made to accommodate the occurrence of transonic points within the integration range.

A. Boundary conditions for perturbations

The sets of ODE's are solved as initial value problems where the initial values for the perturbations are required to be given at some maximum value of r corresponding to radial infinity. These boundary conditions for the perturbations at radial infinity should correspond to the values the perturbations take in the zero-gravity limit. Hence, the boundary conditions assumed here will be the special relativistic results obtained by SK [4]. Of course, numerically these are only an approximation but they do constitute a reasonable set of boundary conditions for a preliminary investigation of the waves. The perturbations in the special relativistic case with no gravity have plane wave solutions so that, for a quantity Ψ,

$$\delta\Psi(r,t) \sim e^{i(kr-\omega t)} , \tag{66}$$

where r now replaces z. In what follows it is assumed that, in general,

$$\delta\widetilde{\Psi}(\tilde{r},\tilde{t}) = \frac{1}{\Psi_{0s}}\delta\Psi(\tilde{r},\tilde{t}) = e^{i\left(\tilde{k}\tilde{r}-\tilde{\omega}\tilde{t}\right)} \tag{67}$$

is a dimensionless perturbation, where $\alpha = 1$.

The values for the wave number $\tilde{k}$ are taken directly from the dispersion relations for the transverse and longitudinal waves, respectively, as derived by SK [4]. Hence, in terms of the dimensionless variables, for the Alfvén and high-frequency transverse waves their Eq. (5.4) takes the form

$$\tilde{k} = \tilde{\omega}\left\{1 - \frac{2\omega_p^2/\omega_*^2}{(\tilde{\omega}^2 - \omega_c^2/\omega_*^2)}\right\}^{\frac{1}{2}} . \tag{68}$$

For the longitudinal waves Eq. (4.9) of SK, in dimensionless variables, may be written

$$\tilde{k} = \frac{\sqrt{2}}{v_T}\left(\tilde{\omega}^2 - 2\frac{\omega_p^2}{\omega_*^2}\right)^{\frac{1}{2}} . \tag{69}$$

Note that this limits consideration to high-frequencies so that $\tilde{\omega} > 1$ where ω_* is chosen to be $\omega_* = \sqrt{2}\omega_p$. In the case of the two-stream instability, matters are more complicated because of the presence of the streaming velocity. The result is obtained from the special relativistic, zero-gravity dispersion relation obtained by Cornish [8] and in dimensionless form is given by

$$\tilde{k}_{\pm}^2 = \frac{1}{(v_0^2 - v_T^2/2)^2}\left\{\tilde{\omega}^2\left[v_0^2\left(1-\frac{v_T^2}{2}\right)^2 + \frac{v_T^2}{2\gamma_0^4}\right] + \frac{\omega_p^2}{\gamma_0^2\omega_*^2}\left(v_0^2 - \frac{v_T^2}{2}\right)\right\}$$
$$\pm\frac{(1-v_0^2)}{(v_0^2 - v_T^2/2)^2}\left\{2v_0^2v_T^2\tilde{\omega}^4\left(1-\frac{v_T^2}{2}\right)^2 + \frac{\omega_p^4}{\omega_*^4}\left(v_0^2-\frac{v_T^2}{2}\right)^2 + \frac{4v_0^2\gamma_0^2\omega_p^2\tilde{\omega}^2}{\omega_*^2}\left(v_0^2-\frac{v_T^2}{2}\right)\left(1-\frac{v_T^2}{2}\right)^2\right\}^{\frac{1}{2}} \quad (70)$$

for an electron-positron plasma where both species have the same densities and are at the same temperature. Because of the nature of the instability in the zero-gravity, special relativistic case, there is no guarantee that the initial conditions as described by the above dispersion relation will yield stable plane wave solutions for all frequencies. If $\tilde{k}$ becomes complex, the boundary values for the perturbations will be described by unstable solutions. All this conspires to make the two-stream instability a more complicated problem to solve. There are two possible choices of $\tilde{k}$ resulting from the above dispersion relation. The one constraint which must hold is that $\mathrm{Re}(\tilde{k}) \geq 0$. In what follows, the stable branch of the zero-gravity result will always be chosen as the initial value for the perturbations.

B. Boundary values for equilibrium parameters

There are various factors which, from a computational perspective, restrict the possible values of the equilibrium number density and temperature imposed as initial conditions at radial infinity.

The main restriction on the density is that a higher density leads to higher values for the plasma frequency and so the rate of oscillation of the resulting waves is so high that it becomes impossible to obtain a reasonable resolution of the data from which to compute the average energy density. This does not affect the Alfvén waves as much as the high-frequency electromagnetic waves or the longitudinal waves since the cyclotron frequency is the characteristic frequency which is used to scale the frequency for the Alfvén waves and its magnitude is largely unaffected by a change in fluid density. If one chooses $\tilde{r}_\infty = 10^4$ and $n_\infty = 1\,\mathrm{cm}^{-3}$ (i.e., interstellar gas density) then one obtains $n_H = 10^6\,\mathrm{cm}^{-3}$. This is unrealistically low for a limiting horizon fluid density but should suffice to give an indication as to the behavior of these waves. A higher density will yield somewhat different results, of course, as will be shown in the case of the Alfvén waves.

The choice of magnetic field at the boundary, however, does affect the value of the cyclotron frequency. In all the cases considered in the present paper, the value of the magnetic field at radial infinity is assumed to be relatively small, that is, $B_\infty = 3 \times 10^{-6}$ G. Again, if radial infinity is taken to be $\tilde{r}_\infty = 10^4$, then the equilibrium field at the horizon will be $B_H = 300$ G. If one chooses $\tilde{r}_\infty = 5000$, then the field at the horizon will be only $B_H = 75$ G. Again, these values are very low. However, the results to follow are of an exploratory nature and are intended to give an indication of the general behavior of these waves. There are endless possibilities for further investigation of the solutions to the various sets of ODE's, but this is left to further work.

The choice of temperature at radial infinity affects the position of the critical points corresponding to the transonic radii of the fluids and so the values which may be chosen as initial temperatures at the outer boundary are limited for the cases being examined in this work. That is, since only cases for which there are no critical points in the integration range are being considered, the boundary temperatures chosen must be low enough to ensure this condition holds. This is not a problem, however, as if $\tilde{r}_\infty = 10^4$, temperatures up to about $T_\infty \sim 10^5$ K can be considered, which results in a horizon temperature of about 10^7 K. If $\tilde{r}_\infty = 5 \times 10^3$ and $T_\infty = 10^5$ K, this gives a horizon temperature of about $T_H \sim 1.58 \times 10^6$ K. For electrons the limiting horizon temperatures are believed to have an upper bound of about 10^8 K [9] and so the above temperatures are not unrealistic. This is really only a problem for the longitudinal waves and the two-stream instability as no critical points occur in the transverse wave equations.

C. Frequency profiles

Recall from Eq. (48) that for the Alfvén waves $\tilde{\omega}$ has been chosen such that $\tilde{\omega} = \omega/(\alpha\omega_c)$ where $\omega_c =$

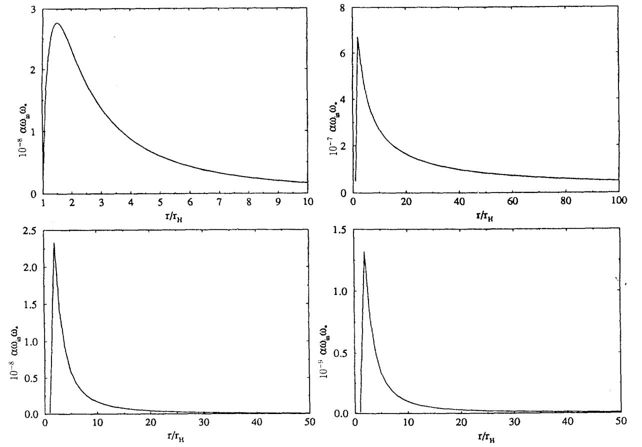

FIG. 1. Frequency profiles for (top left and right): the Alfvén waves with $\omega_{\mathrm{in}} \equiv \tilde{\omega} = 0.25$, (bottom left): the high-frequency transverse frequency waves, and (bottom right): the longitudinal waves with $\omega_{\mathrm{in}} \equiv \tilde{\omega} = 2$. The fluid and field parameters were chosen to be $n_{\infty s} = 1\ \mathrm{cm}^{-3}$, $T_{\infty s} = 10^5$ K, $B_\infty = 3\times10^{-6}$ G, and $\gamma_g = 4/3$, with $\tilde{r}_\infty = 10^4$.

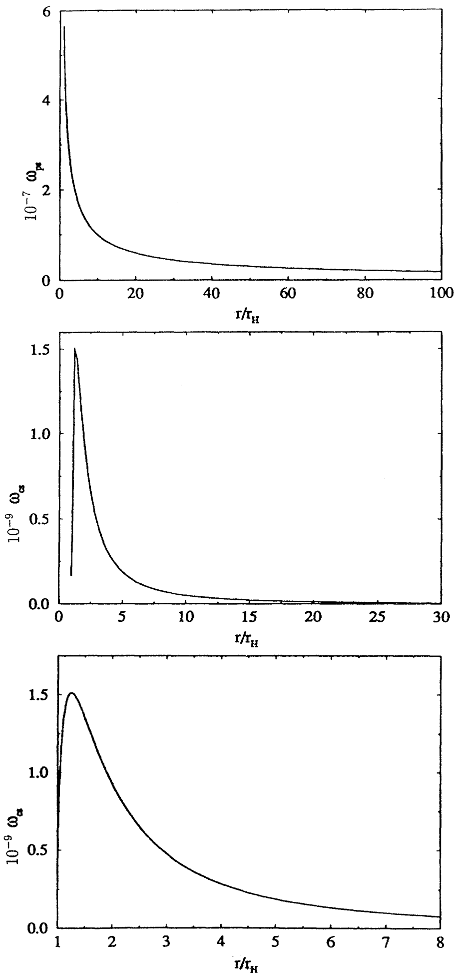

FIG. 2. Profiles of (top): the plasma frequency ω_{ps} and (center and bottom): the cyclotron frequency ω_{cs} for $n_{\infty s} = 1$ cm^{-3}, $T_{\infty s} = 10^5$ K, $B_\infty = 3 \times 10^{-6}$ G, and $\gamma_g = 4/3$, with $\tilde{r}_\infty = 10^4$.

$\left(\omega_{c1}^2 + \omega_{c2}^2\right)^{\frac{1}{2}} / \sqrt{2}$ and for the high-frequency waves $\tilde{\omega} = \omega / \left(\alpha\omega_*\right)$ where $\omega_{*s} = \left(2\omega_{ps}^2 + \omega_{cs}^2\right)^{\frac{1}{2}}$. Figure 1 shows the frequency profiles for the Alfvén, high-frequency transverse, and the longitudinal waves. The top right curve in Fig. 1 shows a closeup view of how the frequency for the Alfvén waves behaves near the horizon. Note that in all three cases the turning point for the frequency occurs at approximately $\tilde{r} = r/r_H \sim 1.5$. Figure 2 shows the plasma frequency and cyclotron frequency profiles. As can be seen from the bottom diagram, the turning point for the cyclotron frequency is about $\tilde{r} \sim 1.25$. Figure 3 displays the scaling frequencies used for the Alfvén, high-frequency electromagnetic, and the longitudinal waves. Although the equilibrium parameters have fairly simple profiles, generally of the form $1/r^q$, they are presented here for completeness and are shown in Fig. 4.

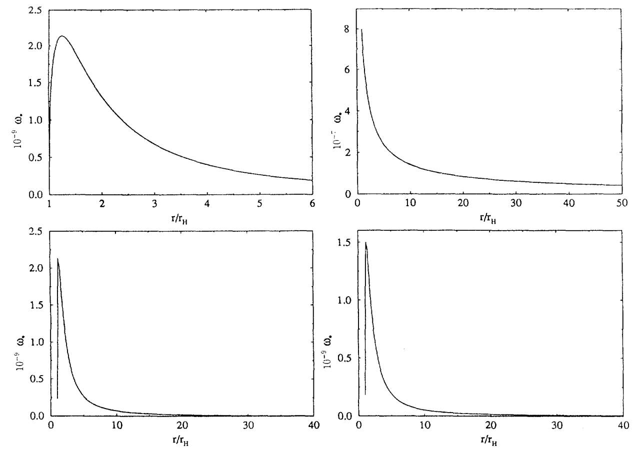

FIG. 3. Profiles for ω_* for (top left): the Alfvén waves, (top right): the high-frequency electromagnetic waves, and (bottom): the longitudinal waves. The fluid and field parameters were chosen to be $n_{\infty s} = 1$ cm^{-3}, $T_{\infty s} = 10^5$ K, $B_\infty = 3 \times 10^{-6}$ G, and $\gamma_g = 4/3$, with $\tilde{r}_\infty = 10^4$.

VIII. COMPONENTS OF THE ELECTRIC AND MAGNETIC FIELD PERTURBATIONS

Because the solutions for the perturbations are rapidly oscillating functions of r, one of the main obstacles in obtaining reasonable solutions is that a large number of data points is required to obtain good resolution. Added to this is the fact that the solutions, in general, oscillate on different wavelength (and, therefore, wave number) scales for much of the r domain. For these reasons, only sampled sections are presented here, to give an impres-

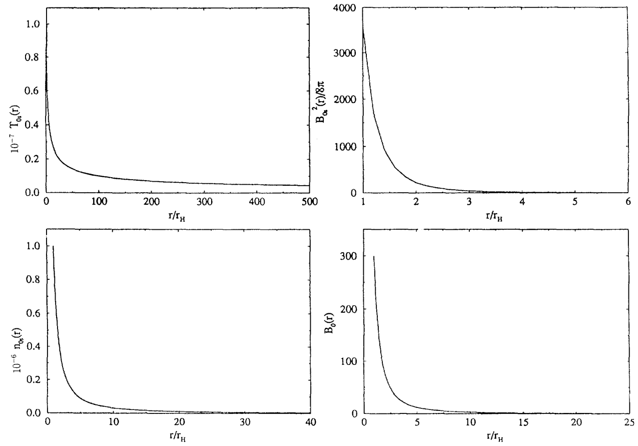

FIG. 4. Profiles of equilibrium parameters for (bottom left): the fluid density, (top left): the temperature profile, (bottom right): the magnetic field profile, and (top right): the equilibrium energy density. The fluid and field parameters were chosen to be $n_{\infty s} = 1$ cm^{-3}, $T_{\infty s} = 1.0 \times 10^5$ K, $B_\infty = 3 \times 10^{-6}$ G, and $\gamma_g = 4/3$, with $\tilde{r}_\infty = 10^4$.

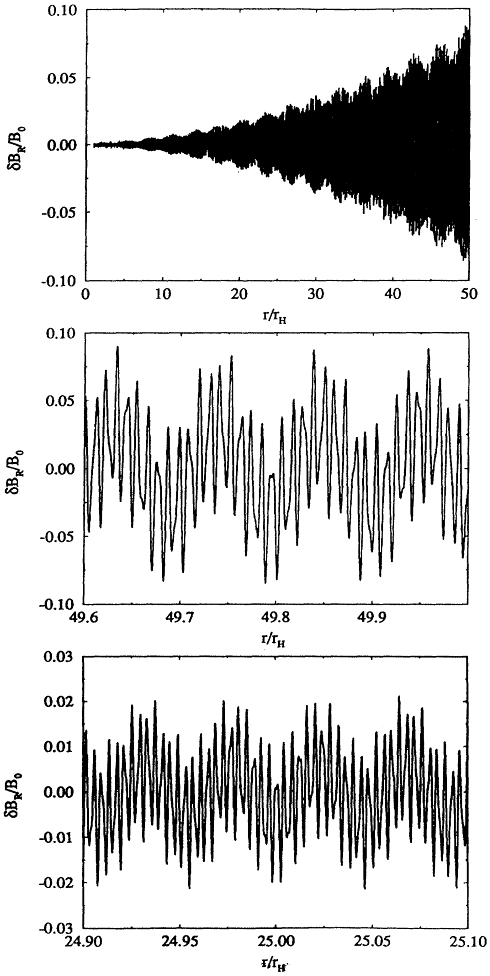

FIG. 5. These are sampled sections of the solutions for the real part of the magnetic field perturbation, $\delta B_R(r)$, for the Alfvén waves. The input parameters were chosen to be $\tilde{r}_\infty = 10^4$, $n_{\infty s} = 1$ cm^{-3}, $T_{\infty s} = 10^5$ K, $B_\infty = 3 \times 10^{-6}$ G, $\gamma_g = 4/3$, $M = 5M_\odot$, and $\tilde{\omega} = 0.25$.

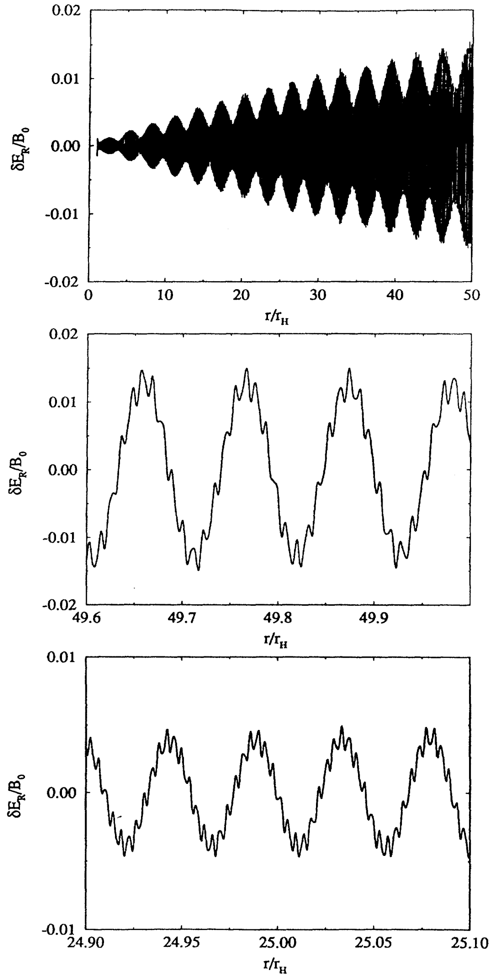

FIG. 6. The real component of the electric field perturbation, $\delta E_R(r)$, for the Alfvén waves, where the input parameters were chosen to be $\tilde{r}_\infty = 10^4$, $n_{\infty s} = 1$ cm^{-3}, $T_{\infty s} = 10^5$ K, $B_\infty = 3 \times 10^{-6}$ G, $\gamma_g = 4/3$, $M = 5M_\odot$, and $\tilde{\omega} = 0.25$.

sion of the nature of the results. In general, for the Alfvén and high-frequency electromagnetic waves, the real and imaginary components of the magnetic field perturbations are essentially the same except for a difference in phase. The same is true of the electric field components. For this reason, only the real components of the electric and magnetic field perturbations will be displayed for the transverse wave results to follow. For all except the longitudinal waves, attention has been restricted to a region relatively close to the horizon, that is, $\tilde{r} < 50$, as this is the most interesting region.

A. Alfvén waves

Two cases are presented for the Alfvén waves, using different starting values for "radial infinity" $\tilde{r}_\infty$, and so also for the equilibrium densities, temperatures, and magnetic field. In the first case the initial conditions are imposed at $\tilde{r}_\infty = 10^4$ with $n_{\infty s} = 1$ cm^{-3}, $T_{\infty s} = 10^5$ K, $B_\infty = 3 \times 10^{-6}$ G, $\gamma_g = 4/3$, $M = 5M_\odot$, and $\tilde{\omega} = 0.25$, where M is the mass of the black hole. Figure 5 shows sampled sections of the solution for the real part of the magnetic field perturbation, $\delta B_R(r)$. The real part of the electric field perturbation, $\delta E_R(r)$, is shown in Fig. 6. As can be seen from these figures, the bulk structure shows large wave packet behavior, which is more evident far from the horizon for the electric field components than for the magnetic field components. Note that the perturbations as depicted in Fig. 5 and Fig. 6 and, indeed, all those which follow, are scaled by the equilibrium magnetic field $B_0(\tilde{r})$ which increases as $\tilde{r}$ decreases (see Fig. 4). Hence, although it appears here as though the amplitudes of the field components are decreasing, they are in fact increasing. Closer to the horizon the solutions for the magnetic field perturbations, and the electric field perturbations become identical; that is, the small wave packet behavior disappears and only the rapid oscillations are left, giving simply sinusoidal oscillations with increasing amplitude as the radius decreases. As can be seen from Figs. 5 and 6 the oscillations occur on different wavelength–wave-number scales, corresponding to the various wave modes. The fact that the small wave packets disappear close to the horizon would seem to indicate that this particular mode dies off in the near-horizon region.

Compare the results for the previous case to the following solutions. Here, the density is chosen to be much greater, thereby causing the frequency of oscillations to be greater as $\tilde{r}$ decreases. That is, $n_{\infty s} = 10^4$ cm^{-3}. Also, radial infinity is chosen to be $\tilde{r}_\infty = 5 \times 10^3$ instead of the previously chosen value of $\tilde{r}_\infty = 10^4$. This gives a limiting horizon fluid density of $n_H = 3.54 \times 10^9$ cm^{-3}. As can be seen from Fig. 7 the solutions for the magnetic field perturbations in this case (only the real component is displayed) are somewhat different to those of Fig. 5. The main difference is that far from the horizon, at least, what appeared as rapid large amplitude oscillations overlaying the main oscillations for the magnetic field perturbations in the first instance, as shown in Fig. 5, are now rapid oscillations with a decreased amplitude but with a higher wave number. The trend as $\tilde{r}$ decreases is essentially the same, however, in that the oscillations are more rapid (an increase in the wave number for all the oscillations) with one mode dying out very close to the horizon. For the electric field perturbation, the real component of which is displayed in Fig. 8, the small-scale oscillations which were superimposed on the large-scale sinusoids in the previous case are so insignificant as to be almost unnoticeable. This is true closer to the horizon as well, with the oscillations which do exist becoming more rapid as before until, very close to the horizon the electric field perturbations are essentially the same as the magnetic field perturbations. This can be seen by comparing Figs. 7 and 8. Note that the bulk structure for the perturbations in this case is also different to the previous case. For both the wavelength of the oscillations decreases markedly as the radius decreases, suggesting that energy is being fed into the waves by the gravitational field.

B. High-frequency electromagnetic waves

As for the Alfvén waves, two cases are considered here. In the first instance the input parameters for the fluids and field are the same as for the first case considered for the Alfvén waves, where radial infinity is chosen to be $\tilde{r}_\infty = 10^4$. The mass of the black hole is again assumed to be $M = 5M_\odot$ and the frequency of oscillation is taken to be $\tilde{\omega} = 2$. The real part of the magnetic field perturbation is shown in Fig. 9. The electric field perturbation is not shown at all as it is identical to the magnetic field perturbation, aside from a slight difference in amplitude. Again, there are several wave modes corresponding to the oscillations at different wavelengths, as can be seen in

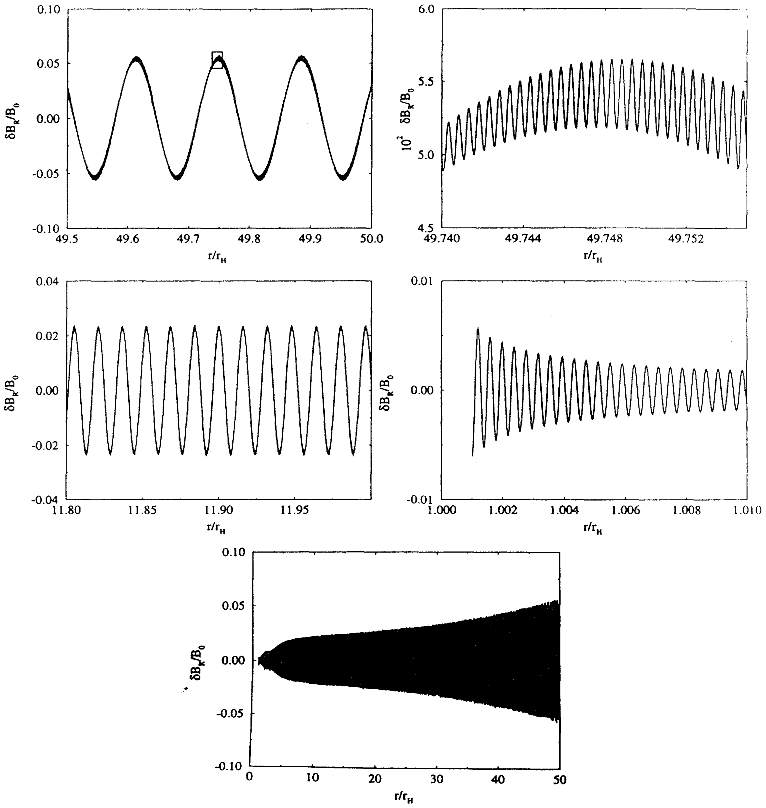

FIG. 7. The real component of the magnetic field perturbation $\delta B_R(r)$ for the Alfvén waves with $\tilde{r}_\infty = 5 \times 10^3$, $n_{\infty s} = 10^4$ cm^{-3}, $T_{\infty s} = 10^5$ K, $B_\infty = 3 \times 10^{-6}$ G, $\gamma_g = 4/3$, $M = 5M_\odot$, and $\tilde{\omega} = 0.25$.

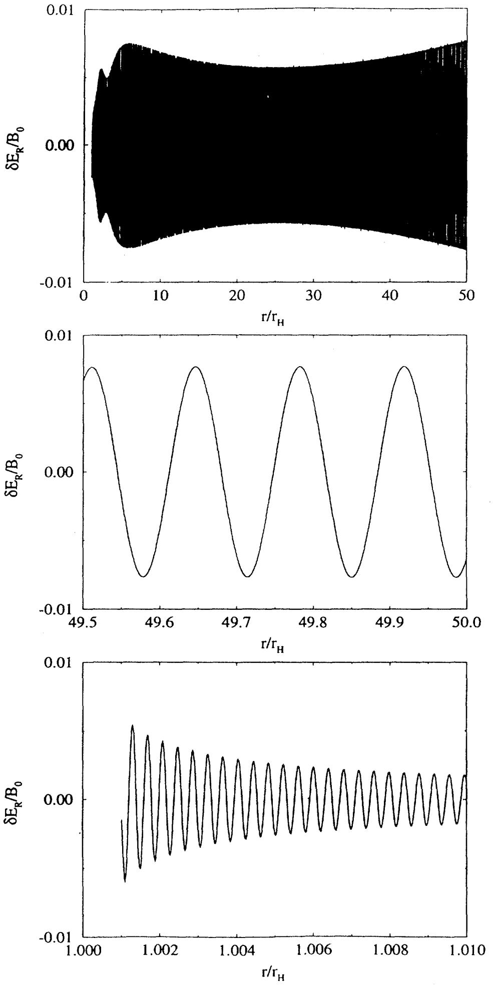

FIG. 8. The real component of the electric field perturbation $\delta E_R(r)$ for the Alfvén waves with $\tilde{r}_\infty = 5 \times 10^3$, $n_{\infty s} = 10^4$ cm^{-3}, $T_{\infty s} = 10^5$ K, $B_\infty = 3 \times 10^{-6}$ G, $\gamma_g = 4/3$, $M = 5M_\odot$, and $\tilde{\omega} = 0.25$.

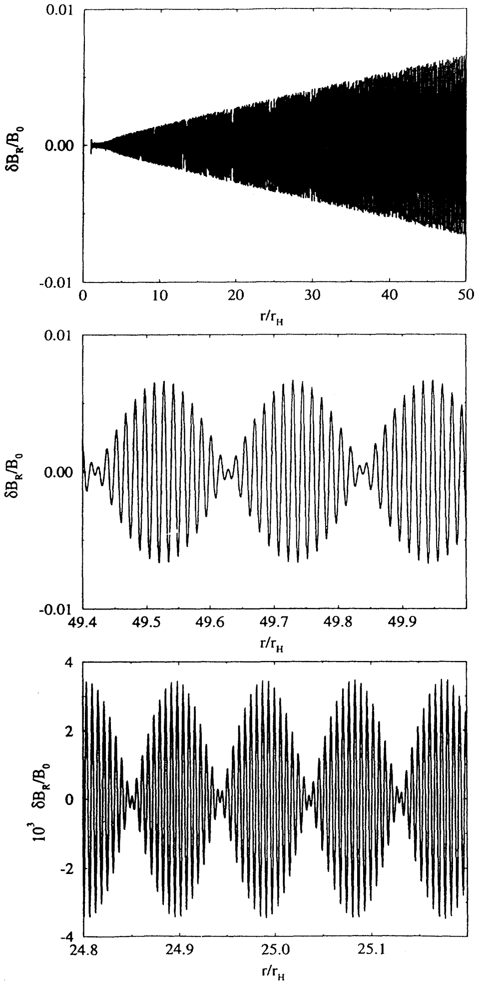

FIG. 9. Real part of the magnetic field perturbation for the high-frequency electromagnetic waves. The input parameters are $\tilde{r}_\infty = 10^4$, $n_{\infty s} = 1$ cm^{-3}, $T_{\infty s} = 10^5$ K, $B_\infty = 3 \times 10^{-6}$ G, $\gamma_g = 4/3$, $M = 5M_\odot$, and $\tilde{\omega} = 2$.

Fig. 9. These become more rapid as the radius decreases because, as before, the frequency of the oscillations will increase, particularly in the region close to the horizon. Very close to the horizon the wave packets again disappear, leaving rapid sinusoidal oscillations, indicating yet again, it would seem, that one of the modes cuts out there. One intriguing feature is the presence of modulations in the wave number (wavelength). These occur more frequently at small radii (that is, very close to the black hole horizon). Two examples of these modulations are shown in Fig. 10. The wave packet modulations are also present to some extent in the solutions for the Alfvén waves but do not occur as frequently and are not as pronounced. These wave number modulations must be due, in some way, to the interaction of the strong gravitational field with the waves. Because the ODE's are so complex, however, it is difficult to relate particular processes in the black hole environment with terms in the relevant equations.

The second case considered for the high-frequency electromagnetic waves has the initial conditions imposed at radial infinity $\tilde{r}_\infty = 5 \times 10^3$ with $n_{\infty s} = 1$ cm^{-3}, $T_{\infty s} = 10^5$ K, $B_\infty = 3 \times 10^{-6}$ G, and $\gamma_g = 4/3$, with the mass of the black hole chosen to be $M = 100M_\odot$ and the frequency $\tilde{\omega} = 2.5$. Hence, the limiting horizon values for the fluid temperatures and densities as well as the equilibrium magnetic field are lower than in the previous case although now the black hole mass is considerably higher. The solutions for the real parts of the magnetic and electric field perturbations are shown in Figs. 11 and 12, respectively. Comparison with Fig. 9 shows that there is no real difference in the structure of the results, apart from differences in wavelength (and therefore also the wave number). Again the electric and magnetic field perturbations are essentially the same and the wavelength modulations still occur (not shown).

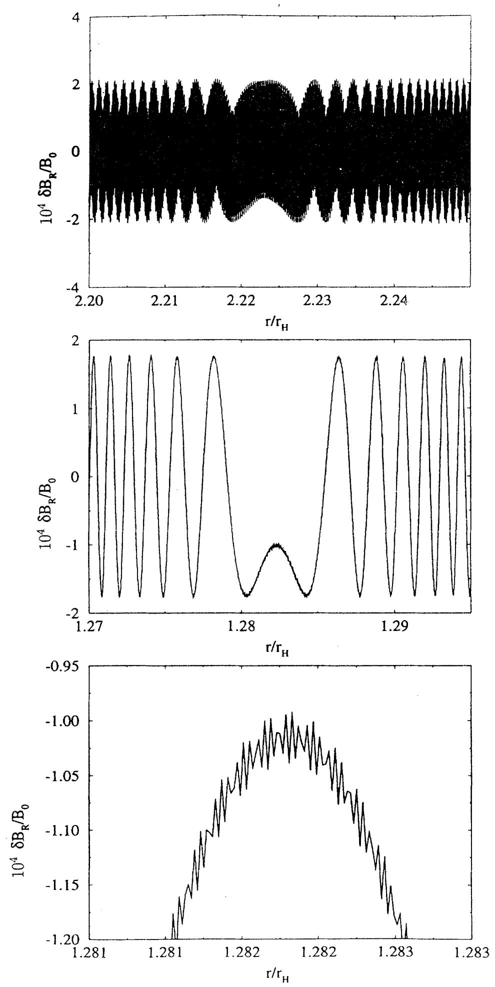

FIG. 10. Sections of the real component of the magnetic field perturbation for the high-frequency electromagnetic waves showing examples of the frequency modulations which occur. The bottom figure is a closeup view of the center figure. The input parameters are $\tilde{r}_\infty = 10^4$, $n_{\infty s} = 1\ \mathrm{cm}^{-3}$, $T_{\infty s} = 10^5$ K, $B_\infty = 3 \times 10^{-6}$G, $\gamma_g = 4/3$, $M = 5M_\odot$, and $\tilde{\omega} = 2$.

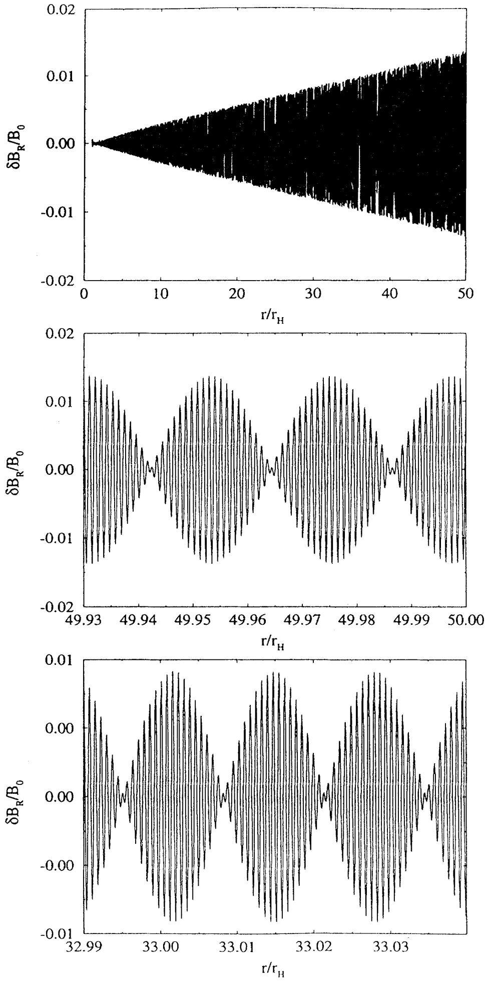

FIG. 11. Real component of the magnetic field perturbation for the high-frequency electromagnetic waves with input parameters $\tilde{r}_\infty = 5 \times 10^3$, $n_{\infty s} = 1\ \mathrm{cm}^{-3}$, $T_{\infty s} = 10^5$ K, $B_\infty = 3 \times 10^{-6}$ G, $\gamma_g = 4/3$, $M = 100M_\odot$, and $\tilde{\omega} = 2.5$.

C. Longitudinal waves

Only one case is considered for the longitudinal waves. Again, radial infinity is chosen to be $\tilde{r}_\infty = 10^4$ and the equilibrium fluid and field values imposed there are the same as for the corresponding cases investigated for the Alfvén and high-frequency electromagnetic waves. The black hole mass is again chosen to be $M = 5M_\odot$ and the frequency is set at $\tilde{\omega} = 2$. Sections of the solution for the real part of the longitudinal electric field perturbation are shown in Fig. 13. The imaginary component is shown in Fig. 14. Unlike the Alfvén or high-frequency transverse waves the longitudinal electric field perturbations do not oscillate about zero. The real component is exclusively negative while the imaginary component is exclusively positive. Very far from the horizon the wavelength modulations which were evident in the transverse waves can also be seen here, in both the real and imaginary components, with the same kind of wave packet behavior superimposed on the main curve. Closer to the horizon, however, this wave packet behavior has disappeared, indicating again that a mode cuts out as the radius decreases. As can be seen from Fig. 14 the oscillations are simple sinusoids in the region close to the black hole horizon with increasing frequency as $\tilde{r}$ decreases and therefore decreasing wavelength. Note the sudden change in slope in both the real and imaginary field components around $\tilde{r} \sim 7.5$. As can be seen from the diagram at the bottom of Fig. 13, this change in slope is simply due to the scaling of the perturbation by the equilibrium magnetic field $B_0(r)$.

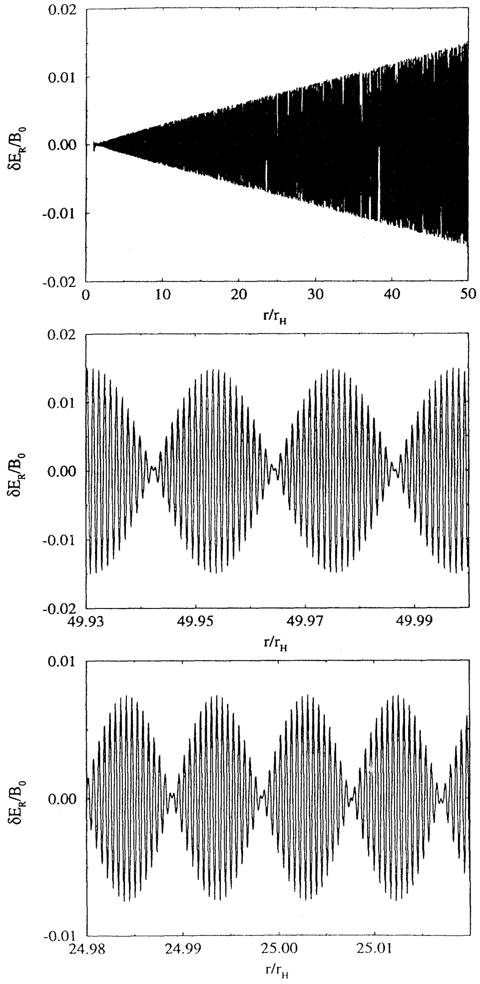

FIG. 12. Real component of the electric field perturbation for the high-frequency electromagnetic waves with input parameters chosen to be $\tilde{r}_\infty = 5 \times 10^3$, $n_{\infty s} = 1\ \text{cm}^{-3}$, $T_{\infty s} = 10^5$ K, $B_\infty = 3 \times 10^{-6}$ G, $\gamma_g = 4/3$, $M = 100 M_\odot$, and $\tilde{\omega} = 2.5$.

D. Two-stream instability

For the test cases investigated for the two-stream instability the initial conditions have consistently been chosen to correspond to the stable branch of the zero-gravity result. Even so, the solutions with gravity become unstable very rapidly at large radii, making it impossible to obtain solutions close to the horizon. As can be seen from Figs. 15 and 16, the solutions become unstable relatively far from the black hole horizon, even for a low streaming velocity.

Two cases are considered here, for low and high-frequencies, respectively. However, only the case of a low streaming velocity is investigated, specifically $v_0 = 0.25 v_{\text{ff}}$. For streaming velocities higher than this the solutions become unstable almost immediately so that it is impossible to obtain meaningful solutions even far from the horizon. This is regardless of whether one begins the calculation at $\tilde{r}_\infty = 10^4$ or $\tilde{r}_\infty = 5 \times 10^3$. Hence, unlike the special relativistic case without gravity (as investigated by Cornish), it appears as though a higher streaming velocity does lead to a stronger instability in the black hole environment. Recall also that the perturbations are scaled by the equilibrium field which is increasing as the radius decreases. Hence, the amplitudes of the field perturbation components are, in fact, growing even more rapidly than they appear to be.

For both cases, radial infinity is chosen to be $\tilde{r}_\infty = 5 \times 10^3$ and the fluid and field parameters imposed there are $n_\infty = 1\ \text{cm}^{-3}$, $T_\infty = 10^5$ K, $B_\infty = 3 \times 10^{-6}$ G, $\gamma_g = 4/3$, and the mass of the black hole is $M = 5 M_\odot$. In the first instance, for the low-frequency case, the frequency is $\tilde{\omega} = 0.5$. The solutions for the real and imaginary longitudinal electric field components are shown in Figs. 15 and 16, respectively. In both cases, as with the longitudinal waves, the solutions do not oscillate about zero until they become unstable. Although the real part is exclusively negative in this region, as for the longitudinal waves, the imaginary part of the longitudinal electric field perturbation is also negative in this relatively stable region. This is in contrast with the longitudinal waves for which the imaginary part of the transverse electric field component is exclusively positive. While the solutions remain stable, they oscillate on two wavelength scales. Below about $\tilde{r} \sim 3500$, however, the solutions become unstable very quickly and the wave packets disappear completely, suggesting that one mode becomes dominant. The solutions then become very rapidly oscillating sinusoids with a dramatically increasing amplitude.

For the second case, the frequency is set at $\tilde{\omega} = 2.5$. The real and imaginary components of the longitudinal electric field perturbation are shown in Figs. 17 and 18. In the region where the solutions are still fairly stable, the solutions for high-frequency are somewhat different to those for the low frequency case in that the wave packet behavior in the low-frequency case is not evident here for high-frequency. In contrast with the low-frequency case, both the real and imaginary parts of the longitudinal electric field perturbation oscillate about positive values in the relatively stable region very far from the horizon. As the solutions become unstable, below $\tilde{r} \sim 3660$, the solutions become identical to those of the low-frequency case and oscillate about zero.

IX. AVERAGE ELECTROMAGNETIC ENERGY DENSITY

From the solutions for the electric and magnetic field perturbations it is possible to compute the average electromagnetic energy density for the various waves in r space. The electromagnetic energy density for the transverse waves is defined as

$$\delta U(r) = \frac{1}{8\pi} \left[|\delta E(r)|^2 + |\delta B(r)|^2 \right] , \qquad (71)$$

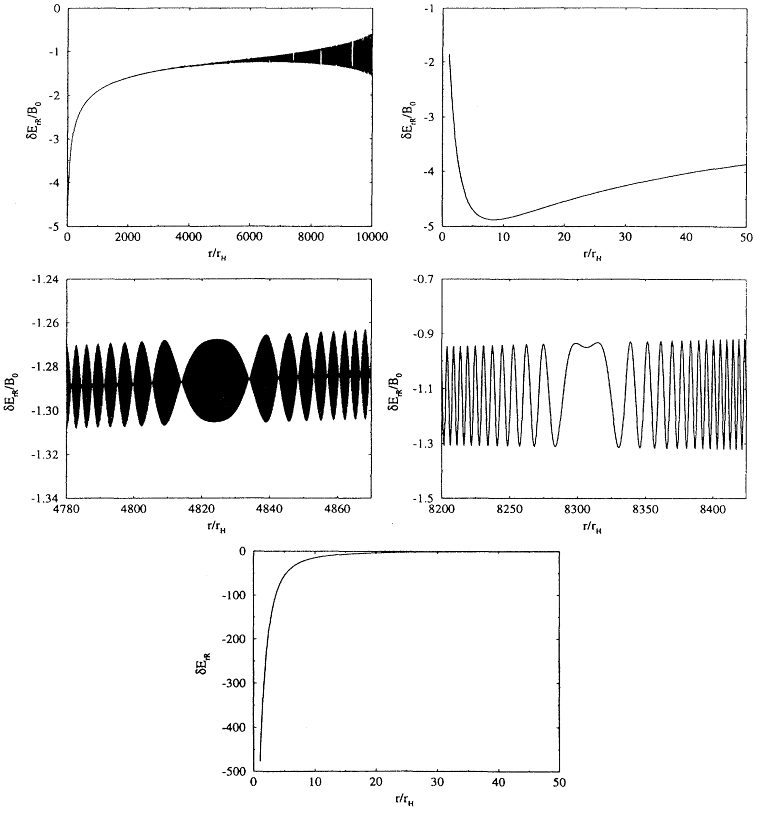

FIG. 13. Real component of the longitudinal electric field perturbation for the longitudinal waves showing (top left): the full solution, (top right): a closeup view of what occurs closer to the horizon, (center left and right): examples of the wavelength modulations which occur far from the horizon, and (bottom): the unscaled electric field perturbation. The input parameters are $\tilde{r}_\infty = 10^4$, $n_{\infty s} = 1$ cm^{-3}, $T_{\infty s} = 10^5$ K, $B_\infty = 3 \times 10^{-6}$ G, $\gamma_g = 4/3$, $M = 5M_\odot$, and $\tilde{\omega} = 2$.

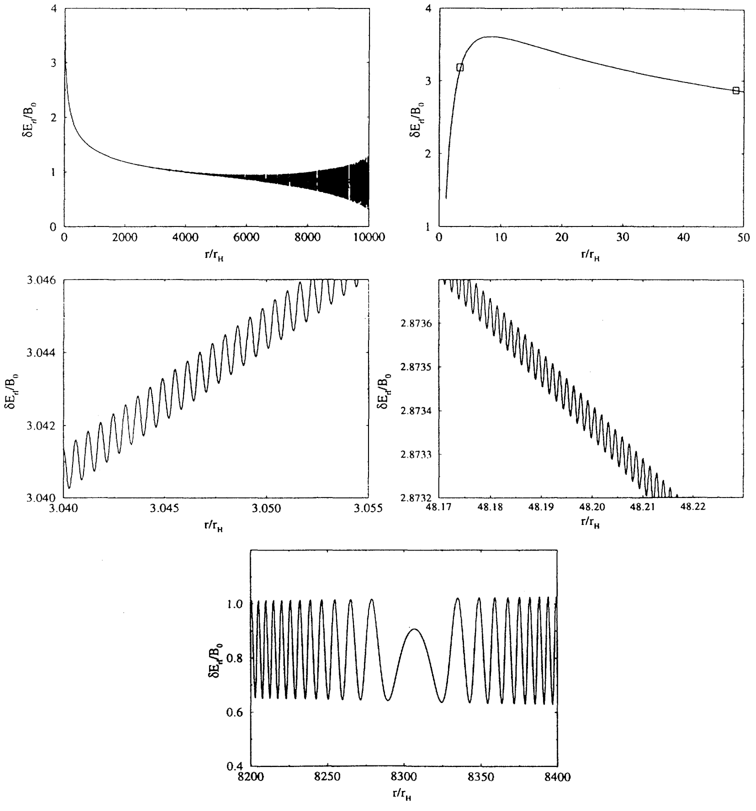

FIG. 14. Imaginary component of the longitudinal electric field perturbation for the longitudinal waves showing (top left): the full solution, (top right): the solution in a region closer to the horizon, (center left and right): boxed sections of the figure at top right, and (bottom): wavelength modulation which occurs relatively far from the horizon. The input parameters are $\tilde{r}_\infty = 10^4$, $n_{\infty s} = 1$ cm^{-3}, $T_{\infty s} = 10^5$ K, $B_\infty = 3 \times 10^{-6}$ G, $\gamma_g = 4/3$, $M = 5M_\odot$, and $\tilde{\omega} = 2$.

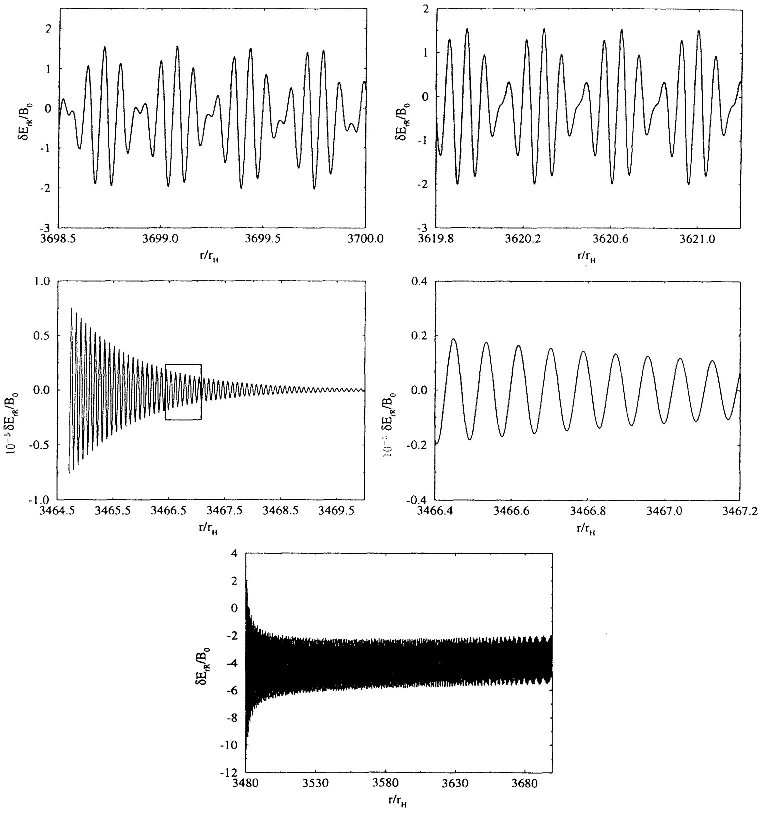

FIG. 15. Real component of the longitudinal electric field perturbation $\delta E_{rR}(r)$ for the two-stream instability with low streaming velocity $v_0 = 0.25 v_{\rm ff}$. The input parameters are $\tilde{r}_\infty = 5 \times 10^3$, $n_{\infty s} = 1~{\rm cm}^{-3}$, $T_{\infty s} = 10^5$ K, $B_\infty = 3 \times 10^{-6}$ G, $\gamma_g = 4/3$, $M = 5 M_\odot$, and $\tilde{\omega} = 0.5$.

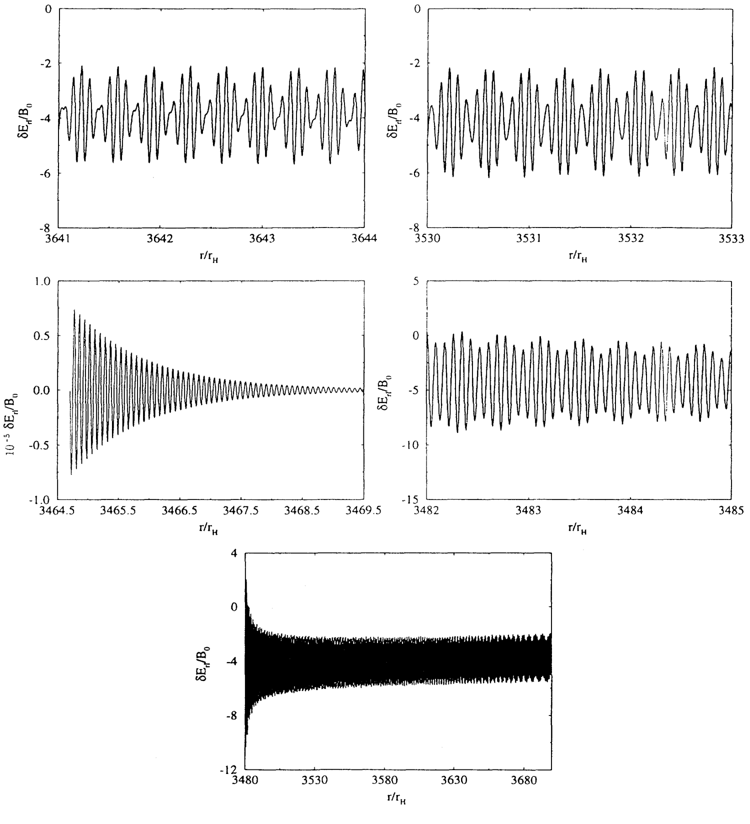

FIG. 16. Imaginary component of the longitudinal electric field perturbation $\delta E_{rI}(r)$ for the two-stream instability with low streaming velocity $v_0 = 0.25 v_{\rm ff}$. The input parameters are $\tilde{r}_\infty = 5 \times 10^3$, $n_{\infty s} = 1~{\rm cm}^{-3}$, $T_{\infty s} = 10^5$ K, $B_\infty = 3 \times 10^{-6}$ G, $\gamma_g = 4/3$, $M = 5 M_\odot$, and $\tilde{\omega} = 0.5$.

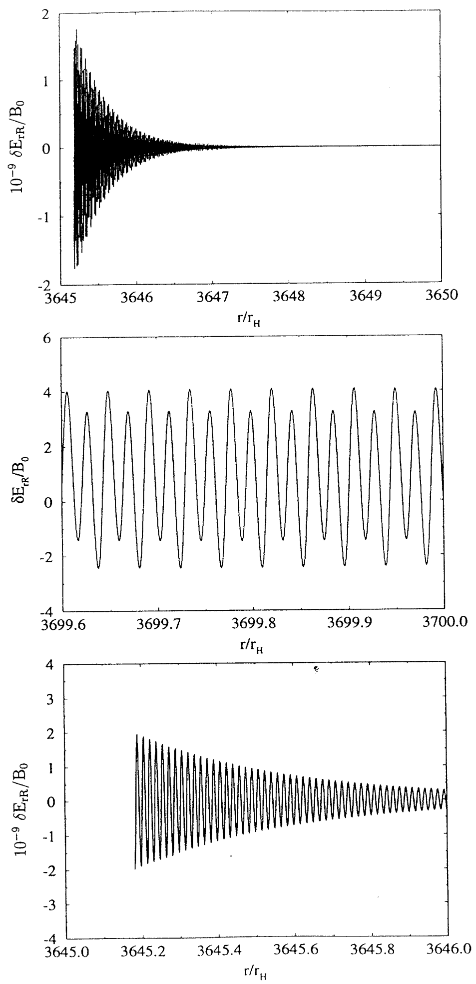

FIG. 17. Real component of the longitudinal electric field perturbation $\delta E_{rR}(r)$ for the two-stream instability with low streaming velocity $v_0 = 0.25 v_{\rm ff}$ and high-frequency. The input parameters are $\tilde{r}_\infty = 5 \times 10^3$, $n_{\infty s} = 1\ \text{cm}^{-3}$, $T_{\infty s} = 10^5$ K, $B_\infty = 3 \times 10^{-6}$ G, $\gamma_g = 4/3$, $M = 5 M_\odot$, and $\tilde{\omega} = 2.5$.

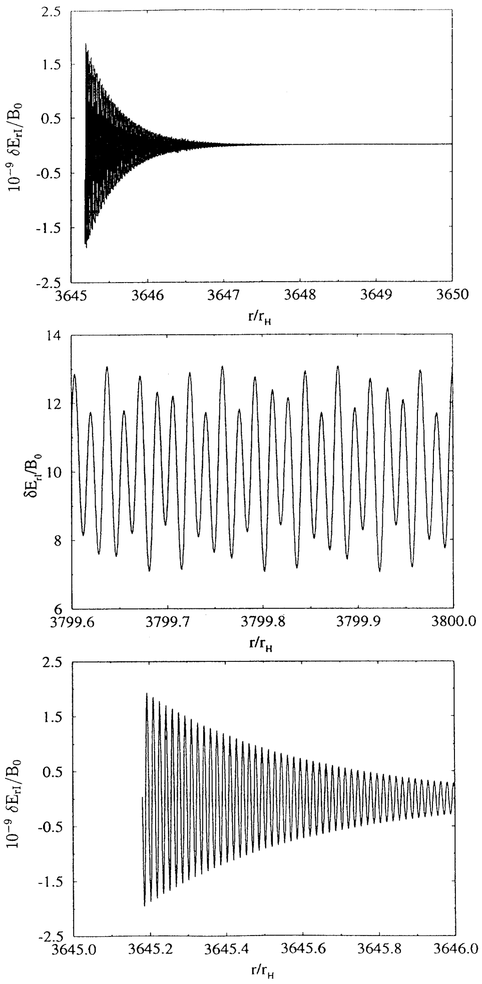

FIG. 18. Imaginary component of the longitudinal electric field perturbation $\delta E_{rI}(r)$ for the two-stream instability with low streaming velocity, $v_0 = 0.25 v_{\rm ff}$ and high-frequency. The input parameters are $\tilde{r}_\infty = 5 \times 10^3$, $n_{\infty s} = 1\ \text{cm}^{-3}$, $T_{\infty s} = 10^5$ K, $B_\infty = 3 \times 10^{-6}$ G, $\gamma_g = 4/3$, $M = 5 M_\odot$, and $\tilde{\omega} = 2.5$.

where $|\delta E(r)|^2 = \delta E_R^2(r) + \delta E_I^2(r)$ and similarly for the magnetic field perturbation. Note that these are not the dimensionless perturbations as defined earlier but simply the perturbations, unscaled by either α or $B_0(r)$. For the longitudinal waves and the two-stream instability, the energy density is simply given by

$$\delta U(r) = \frac{1}{8\pi} |\delta E_r(r)|^2 , \tag{72}$$

where $\delta E_r(r)$ is the longitudinal component of the electric field perturbation.

One can then proceed to obtain the local energy density at each radius $\tilde{r}$ but this varies very rapidly and so is not particularly useful. In order to observe the energy density as it varies with radius it is preferable to compute an average energy density, that is, averaged over some radial interval. This is done by multiplying the signal by a window function centered about some radius r_0 and then dividing by the area under the window function. This results in a relatively smooth spatial average. In this instance, a Gaussian window has been used, normalized such that the area under the window is unity. The Gaussian window function is defined as

$$W(j) = \frac{1}{2\sqrt{\pi N}} e^{-(j-N/2)^2/4N} , \tag{73}$$

where N is the size of the data sample and $W(j)$ is centered about the midpoint radius of the sample, $r_0 \equiv r_{N/2}$. Thus one can compute the average over a data sample of size N as

$$\langle \delta U \rangle = \frac{1}{N} \sum_{j=1}^{N} W(j) \delta U(r_j) . \tag{74}$$

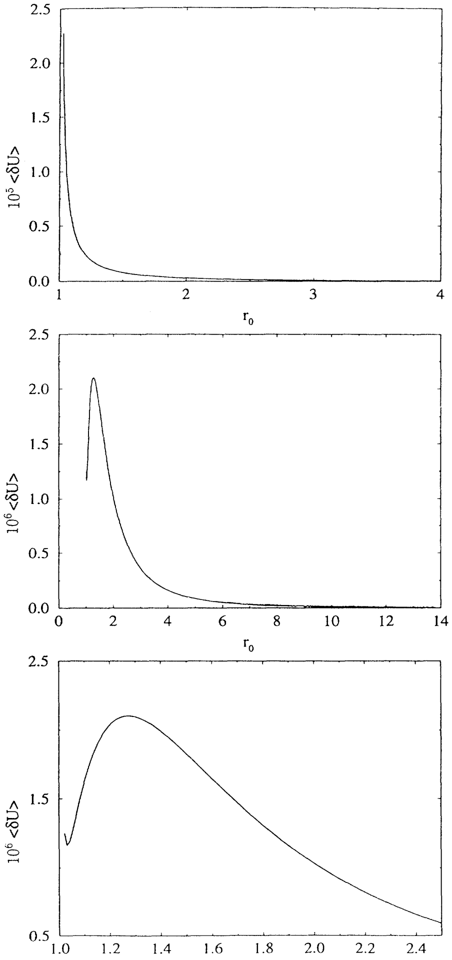

FIG. 19. Average electromagnetic energy densities for the Alfvén waves. Top: the input parameters chosen are $\tilde{r}_\infty = 10^4$, $n_{\infty s} = 1\ \mathrm{cm}^{-3}$, $T_{\infty s} = 10^5$ K, $B_\infty = 3 \times 10^{-6}$ G, $\gamma_g = 4/3$, $M = 5M_\odot$, and $\tilde{\omega} = 0.25$. Center and bottom: the input parameters are $\tilde{r}_\infty = 5 \times 10^3$, $n_{\infty s} = 10^4\ \mathrm{cm}^{-3}$, $T_{\infty s} = 10^5$ K, $B_\infty = 3 \times 10^{-6}$ G, $\gamma_g = 4/3$, $M = 5M_\odot$, and $\tilde{\omega} = 0.25$.

In computing the average energy density for the different waves, the sample size has consistently been chosen to be $N = 1024$. In addition to this, the windows have been overlapped every $N/2$ points in order to obtain an even smoother spatial average. The average electromagnetic energy densities for the Alfvén waves, computed for the two cases shown in Figs. 5–8 are displayed in Fig. 19. As can be seen from the diagrams, the energy density increases dramatically in the region very close to the horizon as the radius decreases. In the second case, however, the energy density suddenly decreases at an average radius of about $r_0 \sim 1.3$ only to increase again almost at the horizon.

The average electromagnetic energy densities for the high-frequency electromagnetic waves, for the cases shown in Fig. 9–12, are displayed in Fig. 20. From these diagrams, it is also clear that the energy density increases sharply very close to the horizon in both cases. The diagrams on the right in Fig. 20 show closeup views of a section of the diagrams on the left. These fine scale variations remain to be explained.

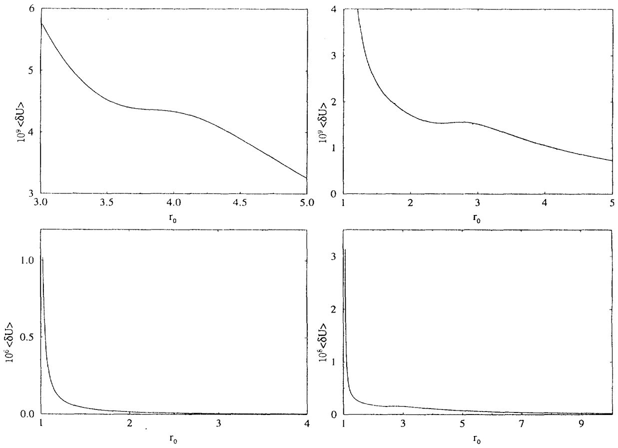

FIG. 20. Average electromagnetic energy densities for the high-frequency electromagnetic waves. Top and bottom left: the input parameters are $\tilde{r}_\infty = 10^4$, $n_{\infty s} = 1\ \mathrm{cm}^{-3}$, $T_{\infty s} = 10^5$ K, $B_\infty = 3 \times 10^{-6}$ G, $\gamma_g = 4/3$, $M = 5M_\odot$, and $\tilde{\omega} = 2$. Top and bottom right: the input parameters are $\tilde{r}_\infty = 5 \times 10^3$, $n_{\infty s} = 1\ \mathrm{cm}^{-3}$, $T_{\infty s} = 10^5$ K, $B_\infty = 3 \times 10^{-6}$ G, $\gamma_g = 4/3$, $M = 100M_\odot$, and $\tilde{\omega} = 2.5$.

The average energy density for the longitudinal waves is shown in Fig. 21. As for the transverse waves, the energy density here increases sharply close to the horizon. The fact that the energy densities do increase so markedly with decreasing radius in the region near the horizon would again seem to suggest that vast amounts of energy are being fed into the waves by the gravitational field. This is consistent with the results obtained in the local approximation in papers I and II.

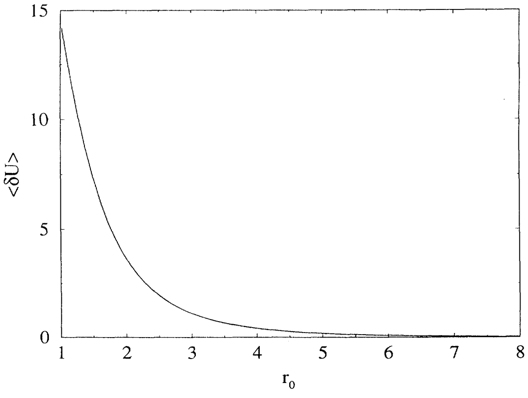

FIG. 21. Average energy density for the longitudinal waves. The input parameters are $\tilde{r}_\infty = 10^4$, $n_{\infty s} = 1\ \mathrm{cm}^{-3}$, $T_{\infty s} = 10^5$ K, $B_\infty = 3 \times 10^{-6}$ G, $\gamma_g = 4/3$, $M = 5M_\odot$, and $\tilde{\omega} = 2$.

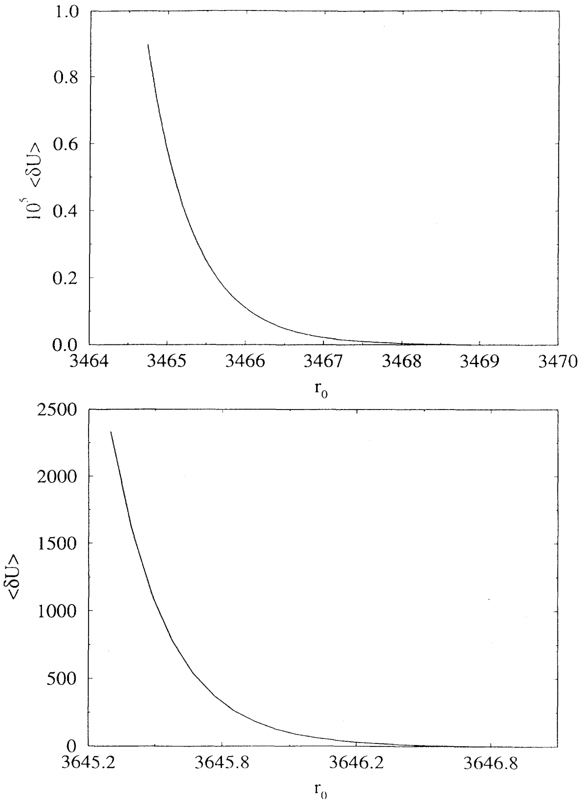

FIG. 22. Average energy densities for the two-stream instability with low streaming velocity $v_0 = 0.25v_{\rm ff}$ and for both (top): low frequency and (bottom): high-frequency. The input parameters are $\tilde{r}_\infty = 5 \times 10^3$, $n_{\infty s} = 1$ cm^{-3}, $T_{\infty s} = 10^5$ K, $B_\infty = 3 \times 10^{-6}$ G, $\gamma_g = 4/3$, $M = 5M_\odot$, and $\tilde{\omega} = 0.5$.

The average energy density for the two-stream instability is shown in Fig. 22 for the low- and high-frequency cases, respectively. As can be seen from the diagrams, the energy density increases dramatically far from the horizon with decreasing radius, as would be expected, given the nature of the solutions for the electric field perturbation. Hence, even far from the horizon, energy is being fed into the waves in a way which indicates the enormous energy content of the black hole's gravitational field as well as the efficiency of the two-stream instability in tapping into this incredible source of free energy.

X. CONCLUSION

In this paper the two-fluid equations are used to obtain two sets of first-order, linear, coupled ordinary differential equations, one set corresponding to the transverse waves and the other to the longitudinal waves. The solutions to these sets of ODE's for simple, idealized scenarios for the electron-positron plasma justify the conclusion from the local approximation (papers I and II) concerning the existence of various modes for each of the wave types. From the computed average electromagnetic energy densities it is clear that in all cases the net effect of the gravitational field through horizon effects is to feed energy into the waves. For the Alfvén, high-frequency electromagnetic, and the longitudinal waves the energy density increases sharply as the region very close to the horizon is approached.

The two-stream instability is interesting in that the solutions become unstable in a region still relatively far from the horizon, even though the stable branch of the zero-gravity result is chosen to define the initial conditions for the perturbations. This is true when the streaming velocity is assumed to be relatively low ($v_0 = 0.25v_{\rm ff}$) compared with the freefall velocity of the fluids and is increasingly so for higher streaming velocities, to the point where the solutions become unstable almost immediately as the distance from the horizon decreases, making it difficult to obtain meaningful numerical results. In contrast to the zero-gravity case investigated by Cornish [8] where the instability tends to die off as the streaming velocity increases, the present work with gravity demonstrates clearly that a higher streaming velocity leads to a stronger instability. From the energy densities computed for the two-stream instability for both low and high-frequencies it is evident that vast amounts of energy are being fed into the waves by the gravitational field. This process is already occurring at a large distance from the horizon, showing that the two-stream instability is indeed an extremely efficient mechanism for energy transfer from the black hole field to the waves.

As can be seen from the results for the Alfvén waves, large changes in the equilibrium density produce significant changes in the final results. A change in the mass of the black hole, however, does not make any significant difference in the results for the field perturbations as is clear from the behavior of the high-frequency waves. However, one would expect some differences if the change in the mass were significant (i.e., many orders of magnitude) as effects due to the horizon are not expected to be important for supermassive black holes [10]. The present work is of an exploratory nature and is intended to give some indication of the types of solutions for the linearized two-fluid equations. An almost endless list of possible physical scenarios exists, limited only by computational requirements.

An investigation of the power spectra of the electric and magnetic field perturbation components would be an interesting extension of the work completed thus far in the solution of the linear ODE's for the various waves. This would be best done using fast Fourier transform techniques. By computing the power spectrum of the electric and magnetic field perturbation components, one would expect to obtain further information about the dispersion relations, specifically more detail concerning the different wave number modes for the various waves.

Another possible extension to the work contained in this paper is to include gravitational effects due to the angular momentum of a Kerr black hole on the two-fluid plasma waves in addition to the waves already investigated here for the Schwarzschild black hole. Although even more complicated than the work contained here, such studies would be important for supermassive black holes which are believed to power active galactic nuclei (AGN's) and quasars [11–13].

One of the most interesting possibilities for future extensions of the present work would be the study of the nonlinear waves and the question of acceleration of particles by plasma waves and the consequent emission of radiation. The aim, as far as the nonlinear waves are concerned, would be to apply the standard nonlinear analysis to the equations already established. One would expect this analysis to be very complicated. It is already clear just how difficult gravitational fields make the analysis of the linear waves. In a nonlinear treatment one would expect to obtain, to first order of nonlinearity, equations which would have solitonlike solutions modified by the effects of the powerful gravitational field. Already in astrophysics there exist soliton-type solutions to nonlinear equations in other environments, such as the pulsar magnetosphere [14] and [15–17]. These solutions give clues as to the types of instability which exist in the relevant medium and to the nature of the quasiparticles which could exist there. At the moment, there is no indication of what to expect as far as nonlinear properties in the black hole environment are concerned.

Of great importance would be the investigation of the acceleration of electrons and positrons by the two-stream instability and the linear plasma waves that have been investigated so far. The consequent emission of radiation, as in the pulsar case [18], should give important indications as to the radiation spectra to be expected in the vicinity of a black hole. With regard to this it is necessary to determine a link between the work done so far on the linear waves, the future work on the nonlinear aspects, and what observational astronomers could be expected to look for. In other words, there remains the unresolved problem of understanding the mechanism by which plasma waves near a black hole give rise to observable radiation emission. The acceleration of charged particles, particularly electrons and positrons, in the electric field of a linear longitudinal plasma wave has been thoroughly investigated by Rowe [18,19]. Applications are given to the pulsar magnetosphere, in which it is supposed that particles accelerated by plasma waves give rise to the coherent radiation emission needed to explain pulsar phenomenology. It could well be that this is also the mechanism required in the context of the black hole plasma. A successful study of the nonlinear plasma phenomena near a black hole and of the linear emission processes resulting from particle acceleration by gravitationally energized plasma waves would lead to results of great significance for astrophysical research.

ACKNOWLEDGMENTS

The authors are grateful to R. A. Treumann for his continued inspiration and support during this work. V. Buzzi wishes to thank L. Berge, now at Murdoch University, Western Australia, and L. Hollenberg at the University of Melbourne for their invaluable advice on numerical techniques. We would also like to thank K. A. Amos at the University of Melbourne for ensuring continued access to adequate computing facilities.

[1] V. Buzzi, K. C. Hines, and R. A. Treumann, this issue, Phys. Rev. D **51**, 6663 (1995).

[2] V. Buzzi, K. C. Hines, and R. A. Treumann, preceding paper, Phys. Rev. D **51**, 6677 (1995).

[3] K. S. Thorne, R. H. Price, and D. A. Macdonald, *Black Holes: The Membrane Paradigm* (Yale University Press, New Haven, CT, 1986).

[4] J. Sakai and T. Kawata, J. Phys. Soc. Jpn. **49**, 747 (1980).

[5] K. S. Thorne and D. A. Macdonald, Mon. Not. R. Astron. Soc. **198**, 339 (1982); D. A. Macdonald and K. S. Thorne, *ibid.* **198**, 345 (1982); R. H. Price and K. S. Thorne, Phys. Rev. D **33**, 915 (1986).

[6] A. C. Hindmarsh, in *Scientific Computing*, edited by R. S. Stepleman *et al.* (North-Holland, Amsterdam, 1983), pp. 55–64.

[7] L. Nobili and R. Turolla, Astrophys. J. **333**, 248 (1988).

[8] N. Cornish, 4th Year Report, University of Melbourne, 1989 (unpublished).

[9] M. Colpi, L. Maraschi, and A. Treves, Astrophys. J. **280**, 319 (1984).

[10] X.-H. Zhang, Phys. Rev. D **39**, 2933 (1989); **40**, 3858 (1989).

[11] M. J. Rees, M. Begelman, R. D. Blanford, and E. Phinney, Nature (London) **295**, 17 (1982).

[12] M. J. Rees, Annu. Rev. Astron. Astrophys. **22**, 471 (1984).

[13] R. D. Blanford and K. S. Thorne, in *General Relativity, An Einstein Centenary Survey*, edited by S. W. Hawking and W. Israel (Cambridge University Press, Cambridge, England, 1979).

[14] J. Sakai and T. Kawata, J. Phys. Soc. Jpn. **49**, 753 (1980).

[15] U. A. Mofiz, Report No. IC/89/176, ICTP, Trieste, 1989 (unpublished).

[16] U. A. Mofiz, Report No. IC/91/178, ICTP, Trieste, 1991 (unpublished).

[17] U. A. Mofiz and A. A. Mamun, Phys. Fluids B **4**, 3806 (1992).

[18] E. T. Rowe, Ph.D. thesis, University of Sydney, 1992.

[19] E. T. Rowe, Aust. J. Phys. **45**, 1 (1992); **45**, 21 (1992).